Transition from stable column to partial collapse during the 79 cal CE P3 Plinian eruption of Mt. Pelée volcano (Lesser Antilles)

Guillaume Carazzo, Stephen Tait, Audrey Michaud-Dubuy, Allan Fries, Edouard Kaminski

Transition from stable column to partial collapse during the 79 cal CE P3 Plinian eruption of Mt Pelée volcano (Lesser Antilles)

Guillaume Carazzo[1,*], Stephen Tait[1], Audrey Michaud-Dubuy[1], Allan Fries[2,3], Edouard Kaminski[1]

[1]Université de Paris, Institut de physique du globe de Paris, CNRS, F-75005 Paris, France

[2]Laboratoire Magmas et Volcans, Université Clermont Auvergne-CNRS-IRD, OPGC, Clermont-Ferrand, France

[3]Now at: Université de Genève, Section of Earth and Environmental Sciences, Genève, Switzerland

*Corresponding author: Guillaume Carazzo, carazzo@ipgp.fr

ORCID Number: orcid.org/0000-0003-0395-2595

Highlights

- We determine the eruptive sequence of the P3 Plinian eruption of Mt Pelée volcano
- New radiocarbon dating measurements provide a refined age of 79 ± 21 cal CE
- We estimate key eruptive parameters of this VEI 5 eruption in the transitional regime
- Increasing eruption rate and decreasing gas content led to partial column collapse
- The transition occurred at conditions well predicted by our 1D theoretical model

Keywords

Mt Pelée volcano, Plinian eruption, tephra fallout, partial collapse, tephrostratigraphy, radiocarbon dating

Abstract

Explosive volcanic eruptions commonly form sustained Plinian columns that collapse at some stage producing dangerous pyroclastic density currents (PDC) on the ground. Numerical and laboratory models of volcanic plumes show that the conditions leading to total column collapse are strongly controlled by the amount of exsolved gas at the source and the mass eruption rate. However, column collapse is rarely total and the volcanic jet often separates in a dense collapsing part feeding PDC and a buoyant rising plume spreading volcanic gases and pyroclasts in the atmosphere. This transitional regime has been directly observed and/or inferred from the structure of the deposits for several past eruptions, but the number of cases for which the partial collapse regime is described in detail, including the 79 CE Vesuvius, and the 186 CE Taupo eruptions, remains too small to fully constrain physical models. Here, we present a detailed reconstruction of the time evolution of the P3 eruption at Mt Pelée volcano (Martinique, Lesser Antilles) that underwent partial column collapse in order to discuss the mechanisms controlling the eruption dynamics and improve the volcanological database on

transitional eruptions. The P3 eruptive succession consists of seven major phases that produced a total of 1 km^3 dense rock equivalent (DRE) of deposits (i.e., VEI 5 event), starting with a thick pumice fall deposit (0.1 km^3 DRE) overlain by alternating pyroclastic density current (PDC) (0.7 km^3 DRE) and pumice fall deposits (0.2 km^3 DRE). We use physical models together with field data on deposit dispersal, thickness, and grain-size distribution to reconstruct the dynamical evolution of the volcanic column. Our results show that the mass eruption rate (MER) increased from 1.2×10^8 to 1.7×10^8 kg s^{-1} during the initial phase producing a 28 to 30 km-high Plinian plume. The MER later reached up to 2.5×10^8 kg s^{-1} and the column entered the partial collapse regime characterized by the formation of a small (i.e., 12 to 17 km-high) ash plume and contemporaneous PDCs mainly channelized in three paleo-valleys. These estimates are used together with published data on magmatic water contents in glass inclusions to decipher the mechanisms leading to partial collapse. The P3 eruption column collapsed due to an increase in mass eruption rate and a decrease in gas content. A similar evolution was also inferred for the 1300 CE P1 and 280 CE P2 eruption deposits, revealing a systematic behavior in the recent Plinian eruptions of Mt Pelée volcano. The comparison of model predictions of column collapse and field data reveals a good agreement for the P1, P2, P3 and Taupo eruptions, but not for the 79 CE Vesuvius eruption where thermal disequilibrium between gas and pyroclasts most likely strongly affected the column dynamics.

1. Introduction

Plinian eruptions are amongst the most powerful and destructive volcanic events on Earth. These explosive eruptions generally form a sustained stable column that can rise up to 40 km in the atmosphere (e.g., the 1991 Pinatubo eruption) and spread out laterally as an umbrella cloud carrying pyroclasts at large distances from the volcano (Koyaguchi and Tokuno, 1993).

64 Abrupt or progressive changes in eruptive conditions at the base of a Plinian column can lead
65 to a radically different behavior in which the column collapses as a turbulent fountain
66 producing hazardous pyroclastic density currents (PDC) that may reach and destroy populated
67 areas (Wilson et al., 2014). One important goal in physical volcanology is to identify the key
68 processes affecting the column stability in order to improve hazard assessment.
69 Recent real-time observations of volcanic plumes and field-based studies on fallout
70 tephra from past eruptions show that explosive eruptions commonly have a complex behavior
71 where both a stable Plinian column and a collapsing fountain feeding PDC are
72 contemporaneous (Carazzo et al., 2015 and references therein). This transitional regime of
73 partial column collapse occurs for Plinian eruptions ranging in size from small to large (e.g.,
74 the 79 CE Vesuvius (Shea et al., 2011), 186 CE Taupo (Wilson and Walker, 1985), 1150
75 Quilotoa (Di Muro et al., 2008), 1912 Novarupta-Katmai (Fierstein and Hildreth, 1992), and
76 1963 Agung (Self and Rampino, 2012) eruptions). Detailed mapping and analysis of eruptive
77 products emplaced during the transitional regime provide valuable data to better understand
78 the mechanisms controlling the partitioning of a Plinian column, and can be used to robustly
79 test numerical and analog models of explosive volcanic eruptions (Di Muro et al., 2004;
80 Carazzo et al., 2015; Suzuki et al., 2016). However, the number of natural cases for which the
81 partial collapse of an initially stable column is described in detail (i.e., in terms of time
82 variation in mass eruption rate, gas content, grain-size distribution and exit velocity) remains
83 too small to fully constrain theoretical models of volcanic plumes (Michaud-Dubuy et al.,
84 2018). With an aim of increasing the inventory of well-constrained past eruptions, we have
85 undertaken a long-term study of the Plinian eruptions of Mt Pelée volcano (Lesser Antilles) as
86 they systematically produced sustained columns that ultimately collapsed (Traineau et al.,
87 1989). Because the Mt Pelée eruptions share many characteristics including similar pre-
88 eruptive magma storage conditions (Martel et al., 1998), they can be used to decipher the

89 mechanisms controlling the behavior of a Plinian plume. In previous studies, we reconstructed
90 the dynamics of the 1300 CE P1 (Carazzo et al., 2012), and 280 CE P2 Plinian eruptions
91 (Carazzo et al., 2019) focusing on the causes for column collapse. We now extend this work
92 to study the P3 eruption deposits whose structure suggests the entrance into the partial
93 collapse regime at some stage of the eruption (Traineau et al., 1989; Wright et al., 2016),
94 making it an excellent candidate to improve the volcanological database on transitional
95 eruptions.

96 The P3 eruption is described in the literature (Roobol and Smith, 1976; Westercamp
97 and Traineau, 1983; Traineau et al., 1989; Wright et al., 2016) but the exact sequence of
98 events and the eruptive parameters are currently poorly known. Here, we use data from a new
99 comprehensive field study together with physical models to reconstruct the detailed time
100 evolution of this eruption and to discuss the mechanisms responsible for the transition from
101 stable column to partial collapse. We identify the eruptive conditions leading to this
102 transitional regime and compare the results to previous work on P3, and on younger Plinian
103 eruptions in Martinique (P1 and P2). We then compare our estimated eruptive parameters for
104 the column at collapse with theoretical predictions from a model of volcanic plumes.
105

106 **2. Overview of the P3 eruption**

107 The P3 deposits were first identified by Roobol and Smith (1976) as a thick pumice fallout
108 unit on the western flank of Mt Pelée volcano standing above the 2406 and 2447 yr BP
109 horizons of their stratigraphic sections. Westercamp and Traineau (1983) provided the first
110 age, synthetic stratigraphic section and distribution map of the P3 deposits (Fig. 1a). The P3
111 Plinian eruption is currently dated at 2010 ± 140 yr BP based on the average of five ^{14}C ages
112 (Westercamp and Traineau, 1983; Traineau et al., 1989). According to these studies, the
113 eruption began with the formation of a sustained Plinian column that covered the western

flank of the volcano with a meter of coarse lapilli, lithic-rich, pumice fallout deposit (phase $P3_1$). This initial stage was immediately followed by the production of high-concentration PDC in the Grande Savane, Habitation Depaz and Falaise River paleo-valleys (Fig. 1a). The second eruptive phase identified by Westercamp and Traineau (1983) consisted of a sustained Plinian column that spread fine lapilli pumice to the south with a striking elongated axis of dispersion (phase $P3_2$). The P3 eruption ended up with the formation of a pumice ash-rich bed (phase $P3_3$) interbedded with high-concentration PDC deposits (Fig. 1a). Later, Traineau et al. (1989) excluded the second phase ($P3_2$) whose distal deposits were found below tephra from an eruption older than $P3_1$. Recent work by Michaud-Dubuy et al. (2019) confirmed that the deposits named $P3_2$ by Westercamp and Traineau (1983) are not interbedded between $P3_1$ and $P3_3$ but belong to a much older event, the 13.5 ka cal BP Bellefontaine Plinian eruption.

Wright et al. (2016) studied the distal products of a Plinian eruption dated between 1800 and 2200 yr BP (their subunit d), which corresponds to the P3 eruption identified by Westercamp and Traineau (1983). Their synthetic stratigraphic section includes a basal pumice-rich low-concentration PDC (named 'surge') deposit overlain by a pumice fallout deposit interbedded with high-concentration PDC (named 'flow') and low-concentration PDC (named 'ash hurricane') deposits. According to their distribution map of the deposits (Fig. 1b), the high-concentration PDC flowed in the Fond Canonville valley, Grande River, Bijou River, and Falaise River, whereas the low-concentration PDC that elutriated from the top of the current spread on hills at distances up to 20 km from the vent. Isopachs of the pumice fallout deposit exhibit a SSW elongation (Fig. 1b), in good agreement with the one inferred by Westercamp and Traineau (1983) (Fig. 1a). Wright et al. (2016) interpreted their complete stratigraphic succession as resulting from the partial and final collapse of an initially stable Plinian column.

The eruptive parameters of the P3 event are currently poorly constrained. Volume estimates for the fallout tephra of the P3 eruption yield a relatively small value of 0.19 km^3 dense rock equivalent (DRE) (Traineau et al., 1989). The direction of tephra dispersal during the initial phase ($P3_1$) suggests that the column was affected by low altitude tropospheric winds, and thus was certainly more than 6 km (Traineau et al., 1989), but no more than 12 km in height (Wright et al., 2016). Such a large uncertainty on the maximum column height makes it difficult to estimate its mass eruption rate. Overall, these sparse and loosely constrained data cannot be used to understand the conditions leading to column collapse.

3. Methodology

3.1. Fieldwork

We identified the P3 eruption deposits at 102 locations in Martinique (Fig. 2). In most cases, these deposits are easily recognizable by their strong internal layering, the abundance of juvenile and accidental lithic fragments in the pumice fallout units, and the presence of the P1 and/or P2 deposits above them (Carazzo et al., 2012; 2019). The P3 outcrops are distributed all around the volcano except to the northwest where exposure is very limited due to dense tropical forest and difficult conditions of access. The thickness of each layer of P3 was measured at every site in order to construct isopach maps. We also excavated a standard 25 x 20 cm area of each fall layer and measured the major axes of the five largest lithic fragments found in order to produce isopleth maps.

3.2. Radiocarbon dating

We dated four charcoals sampled within the P3 deposits at sites 6 (unit A-G), 97 (unit A), 178 (unit A), and 180 (unit A-G), and a paleosol sampled beneath unit A at site 145 (see locations in Fig. 2 and unit descriptions in section 4.1) in order to refine the age of the P3 eruption.

Ages were determined using accelerator mass spectrometry at the LMC14 (Artemis, Laboratoire de Mesure du Carbone 14, CEA Saclay, France), and calibrated using the free software OxCal 4.3 (Bronk Ramsey, 2009) with the atmospheric IntCal13 calibration curve commonly used for the Northern hemisphere (Reimer, 2013). The radiocarbon ages obtained for our stratigraphically-constrained samples were combined with those of Westercamp and Traineau (1983) and validated using the R_combine function of Oxcal and χ^2 test prior to calibration (Ward and Wilson, 1978).

3.3. Grain-size analysis

We carried out grain-size analyses on twenty samples from ten locations representative of the seven different units (A to G) (see Table 1). The samples were dried for 24 h in an oven and sieved by hand down to 6ϕ. We separated the lithic fragments from the pumices by hand in the size range −6ϕ to −4ϕ, and used a binocular microscope to discard crystals and lithic fragments in the size range −4ϕ to −2ϕ. Volume calculations for isomass maps for each ϕ interval were then used to determine the grain-size distributions of single sub-layers. The total grain-size distribution was estimated from the total mass in sieve class ϕ, M_ϕ, by the volume integral (Kaminski and Jaupart, 1998)

$$M_\phi = \int_0^L h(l)\, C_\phi(l)\, A(l)\, \mathrm{d}l, \qquad (1)$$

where $h(l)$ is the deposit thickness, $C_\phi(l)$ is the concentration of class ϕ at distance l from the vent, $A(l)\mathrm{d}l$ is the area bounded by isopachs at distances l and l+dl, and L is the distance where h or C_ϕ drop to zero. We used linear interpolations for h and C_ϕ between the localities.

The cumulative frequency curves were determined assuming a power-law size distribution of the rock fragments (Turcotte, 1986; Kaminski and Jaupart, 1998), where the number of particles with a radius larger than r is given by:

$$N(R_p \geq r_p) = \lambda r^{-D}, \quad (2)$$

with D the power-law exponent that commonly varies between 2.9 and 3.9 for Plinian eruptions (Girault et al., 2014). Because fragmentation is a size-invariant process, the exponent D can be estimated accurately using any sufficiently large range of sizes. Thus, the lack of fine particles lost out at sea does not affect our estimations of D.

3.4. Eruptive parameters

The volume of tephra fallout produced during an explosive eruption can be inferred using several methods based on the thinning trend of the deposit with distance from the source. Here, we used the exponential, power-law and Weibull fits (Pyle, 1989; Bonadonna and Houghton, 2005; Bonadonna and Costa, 2012) computed using the AshCalc software (Daggit et al., 2014). Bearing in mind that only proximal and furthermore incompletely preserved deposits are available in Martinique, the calculated volumes of fall deposits should be taken as minimum estimates. The volume of dilute PDC deposits was calculated using the observed relationship between the volume and area covered by dilute PDC (Dade and Huppert, 1998; Calder et al., 1999), as in Carazzo et al. (2012, 2019) for the P1 and P2 eruptions. The volume of dense PDC was calculated using the product of the average thickness and area covered by the dense PDC. This method is bound to provide minimum estimates since only proximal and furthermore incompletely preserved deposits are available in Martinique.

The maximum column heights associated with the fall deposits were estimated from the distribution of lithic fragments on our isopleth maps using the method of Carey and Sigurdsson (1986). Error bars were calculated using the three values of maximum height inferred from the 8, 16, and 32-mm isopleths (see Fig. 17 in Carey and Sigurdsson, 1986). The alternative method of Bonadonna and Costa (2013) based on variations of grain size with the distance from the source was also used to confirm the robustness of the estimates.

The mass discharge rate feeding the eruption during phases of stable column was inferred from a given column height by using the empirical relationship from Mastin et al. (2009) and the predictions of the model of Girault et al. (2016), which explicitly includes the effect of total grain-size distribution on the plume dynamics. Calculations were made for tropical atmospheric conditions and for a crystal-bearing rhyolitic magma (andesitic bulk composition) with an initial temperature of 1,150 K (Martel and Poussineau, 2007) and a dense rock density of 2,400 kg m^{-3} (Traineau et al., 1989). The mass discharge rates for the collapsing phases were calculated using the model of Bursik and Woods (1996), which treats pyroclastic density currents as supercritical dilute suspensions entraining air as they propagate. Doyle et al. (2010) showed that this assumption is valid for tall, fine-grained column collapses, for which the flow slowly transfers its mass to the dense basal flow. The model of Bursik and Woods (1996) is thus relevant for collapsing phases characterized by the formation of dilute PDC deposits, and was used here.

4. The P3 eruptive succession

4.1. Stratigraphy

Fig. 3a shows a composite stratigraphic section of the P3 deposits, divided into seven major phases based on diagnostic stratigraphic and lithofacies associations, which we describe in more detail below.

4.1.1. Unit A

The stratigraphic succession begins with a layer of clast-supported, coarse white pumice lapilli (Fig. 4a-d). Unit A contains juvenile and accidental lithic fragments in a total amount that typically increases from ≈20 wt.% at base to ≈25 wt.% at top (Fig. 3c). At most sites,

median pumice size remains relatively constant, whereas both the maximum lithic size and the sorting increase from base to top (Fig. 3b-c).

In the downwind direction (to the southwest), unit A has a maximum thickness of 180 cm at 4.5 km from the crater (Fig. 4c). In the crosswind direction, unit A is 130 cm thick at 4.6 km, and steadily thins to 50 cm within 6.1 km of the crater (Fig. 4d). The relatively widespread nature of this deposit, its uniformly decreasing thickness with distance from the source, its clast-supported framework, and its pumice and juvenile lithic fragments characteristics identify unit A as a fall deposit.

4.1.2. Unit B

Unit B consists of light brown fine ash material in which pumice, lithic fragments and crystals are dispersed in a matrix of dense, angular, glass fragments (Fig. 4b, c, e). Most clasts range in size from fine to coarse ash but a few large pumices are present (Fig. 3b). The total amount of lithic fragments in unit B commonly reaches ≈28 wt.%. Where unit B is present, the contact with the underlying layer is sharp, which suggests that there was no time break between deposition of the two units.

Unit B varies irregularly in thickness with distance from the source, and ranges from 18 to 35 cm at 3.8 km from the eruptive center (Fig. 4), but is absent beyond 7 km from the vent. Where thick, unit B contains a few lenses of coarse lapilli, angular to sub-rounded pumices. At some sites in valleys, pumice lapilli and blocks are rounded and account for a large proportion in the matrix of white fine ash. The relatively limited dispersal of this unit, its irregular thickness, matrix-supported framework and grain types (juvenile and accidental lithic fragments), as well as the nature of the lower contact, indicate that unit B is a low-concentration pyroclastic density current deposit (Branney and Kokelaar, 2002).

261 4.1.3. Unit C

262 Unit C is a relatively thin blanket of clast-supported, white pumice lapilli (Fig. 4b, c, e)
263 containing juvenile and accidental lithic fragments in a total amount that reaches ≈25 wt.% in
264 most studied outcrops (Fig. 3c). At most field sites, unit C is easily distinguishable from unit
265 A, the former being distinctly richer in lithic fragments and coarse lapilli pumice. The
266 maximum lithic size in unit C is, however, always lower than the maximum lithic size at the
267 top of unit A (Fig. 3c).

268 Unit C was dispersed in approximately the same direction as unit A, and is the thickest
269 ≈3.7 km southwest of the volcano in the downwind direction, where it reaches 22 cm. This
270 layer steadily thins with distance from the vent, and is still 10 cm thick at 6.2 km in the
271 crosswind direction. At most sites, the upper part of unit C was eroded by the pyroclastic
272 density current that overrode it and deposited unit D (see below). The relatively widespread
273 nature of unit C, its uniformly decreasing thickness with distance from the source, its clast-
274 supported framework, and its pumice and juvenile lithic fragments characteristics identify it
275 as a fall deposit.

276

277 4.1.4. Unit D

278 Unit D is a relatively thin layer of fine ash and small rounded pumice lapilli dispersed in a
279 matrix of dense, angular, glass fragments (Fig. 4a, c, f). At distal sites, this layer is thin,
280 stratified and unconsolidated. The total amount of lithic fragments in unit D commonly
281 reaches ≈20 wt.% (Fig. 3c). Where unit D is present, the contact with the underlying layer is
282 sharp and exhibits some erosion of unit C.

283 Unit D varies irregularly in thickness with distance from the vent, and ranges from 5 to
284 17 cm at 3.8 km from the volcano (Fig. 4). This layer is, however, absent beyond 7 km from
285 the vent. These irregular thicknesses, the relatively limited dispersal of this deposit, the clast

and matrix types, and the nature of the lower contact indicate that unit D is a low-concentration pyroclastic density current deposit.

4.1.5. Unit E

Unit E is a layer of clast-supported, white pumice lapilli (Fig. 4b, c, e) containing juvenile and accidental lithic fragments in a total amount that typically reaches ≈18 wt.% (Fig. 3c). At most sites, both the median grain-size and the maximum lithic size are lower than those measured in unit C (Fig. 3c).

Material was dispersed in approximately the same direction as units A and C to the southwest of the volcano. The maximum thickness is 13 cm at 3.7 km, and steadily thins to 9 cm within 4.8 km from the vent in the downwind direction. The full thickness of unit E is however poorly preserved due to significant erosion by the overlying pyroclastic density current that overrode it and deposited unit F (see below). The relatively widespread nature of this deposit, its uniformly decreasing thickness with distance from the source, its clast-supported framework, and its pumice and juvenile lithic fragments characteristics identify unit E as a fall deposit.

4.1.6. Unit F

Unit F is a matrix-supported layer of fine to coarse ash containing rounded pumice lapilli and lithic fragments (Fig. 4b, f), the latter of which typically reaches ≈15 wt.% (Fig. 3c). Where unit F is present, the contact with the underlying layer is sharp and exhibits some erosion of unit E.

Unit F varies irregularly in thickness with distance from the vent depending on the topography, ranges from 6 to 75 cm at 3.8 km from the volcano, and is absent 7 km from the vent (Fig. 4). The relatively limited dispersal of this unit, its irregular thickness, matrix-

311 supported framework and grain types (juvenile and accidental lithic fragments), as well as the
312 nature of the lower contact, indicate that unit F is a low-concentration pyroclastic density
313 current deposit.
314
315 4.1.7. Unit G
316 Unit G is the uppermost layer in the P3 sequence and consists of a blanket of fine to coarse
317 white pumice lapilli (Fig. 4a, b, f). This unit contains juvenile and accidental lithic fragments
318 in a total amount that reaches ≈20 wt.% at most studied outcrops (Fig. 3c) with a maximum
319 lithic size similar to that of unit C (Fig. 3c).
320 In the downwind direction (to the southwest), unit G has a maximum thickness of 80
321 cm at 1.4 km from the crater, and steadily thins to 20 cm within 4.8 km of the vent. In the
322 crosswind direction, unit G is 30 cm thick at 5 km, and 15 cm at 6.4 km from the vent. The
323 relatively widespread nature of this deposit, its uniformly decreasing thickness with distance
324 from the source, its clast-supported framework, and its pumice and juvenile lithic fragment
325 characteristics identify unit G as a fall deposit.
326
327 4.2. Age of the P3 eruption
328 Radiocarbon dates and calibrated ages are reported in Supplementary material Table S1. Two
329 samples provide the exact same radiocarbon age of 1,870 ± 30 yr BP (sites 145 and 178 on
330 the western flank). A third sample taken near location 178 gives a radiocarbon age of 1,915 ±
331 30 yr BP (site 97). The oldest age is found near the town of Le Carbet where the charcoal
332 sampled within the pumice fallout deposit provides an age of 2,030 ± 30 yr BP. On the
333 eastern flank of the volcano, the charcoal sampled at location 6 has an age of 1,795 ± 30 yr
334 BP. These five new radiocarbon ages are in good agreement with a compilation of twelve ^{14}C
335 ages determined in previous studies (Walker, 1973; Roobol and Smith, 1976; Traineau, 1982;

336 Westercamp and Traineau, 1983) ranging from 1,800 to 2,150 yr BP (Supplementary material
337 Table S1). Combining these seventeen values using the R_combine function of OxCal (Bronk
338 Ramsey, 2009) provides an age of 1,926 ± 11 yr BP for the P3 eruption. We note that the χ^2
339 test fails here most likely due to the large number of individual measurements. However, a
340 reasonable correction on the error bar of each dating by a factor of 2 is enough to successfully
341 pass the χ^2 test, reinforcing the confidence that all these otherwise stratigraphically-
342 constrained samples belong to the same eruption. Our new refined radiocarbon age for the P3
343 eruption stands in the lower error bars of the 2,010 ± 140 yr BP proposed by Traineau et al.
344 (1989). Correcting our new estimate with the IntCal13 calibration curve (Reimer, 2013)
345 available in OxCal gives a mean calendar age of 79 ± 21 cal CE (i.e., 31-37 cal CE at 1.7%
346 probability and 51-125 cal CE at 93.7% probability).
347
348 4.3. Grain-size distribution of selected samples
349 Twenty samples from the P3 units were analyzed (Table 1) in order to discuss the evolution of
350 the grain-size distribution during the entire P3 eruption at a single outcrop (Fig. 3), and to
351 determine the total grain-size distribution for the lapilli fraction of unit A deposits (see section
352 4.6). The objective is twofold: to confirm the fall or flow nature of the P3 units, and to
353 estimate the amount of gas trapped in pumice fragments at the beginning of the eruption (see
354 section 6.3). A detailed analysis of the pumice textures is beyond the scope of this paper and
355 can be found in Martel and Poussineau (2007).
356 The fourteen samples from unit A display the typical fallout characteristics with
357 median diameter ranging from 0.7ϕ to -3.3ϕ, and sorting ranging from 1.4 to 2.7. These
358 values are relatively close to those obtained by Bardintzeff et al. (1989) who measured
359 median diameter and sorting ranging from -0.3ϕ to -3ϕ, and 1.7 to 2.8, respectively. Most of
360 the samples collected on land belong to proximal deposits since the medial and distal deposits

were lost at sea. The grain-size distribution of individual samples is systematically bimodal (Fig. 3b) and the amount of ash particles (< 2 mm) always increases from base (≈9 wt.%) to top (≈36 wt.%). The top of unit A is thus always more poorly sorted than the base, but the median grain-size remains approximately constant throughout the unit (Fig. 3c).

The six samples from units B to G collected at outcrop 163 show that units C, E, and G have typical fallout characteristics similar to unit A. The median diameter for these units ranges between -0.1ϕ and -3ϕ, and they have moderate sorting values from 2.5 to 2.7 (Fig. 3c). The amount of ash-sized particles is similar to or larger than in unit A, ranging from ≈28 wt.% to ≈55 wt.%. Units B, D, and F have flow features with median diameter ranging from 1.7ϕ and 0.4ϕ, and moderate sorting ranging from 2.2 to 2.6 (Fig. 3c). The amount of ash-sized particles is larger than in the fall deposits, ranging from ≈62 wt.% to ≈85 wt.%.

4.4. Isopach maps

Fig. 5 shows a stratigraphic correlation of P3 outcrops along three different dispersal axes (i.e., north to south, northwest to southeast, and northeast to southwest, see Fig. 2 for localization). The complete sequence can be found up to 5 km from the vent (sites 13, 163, 101, 78 in Fig. 5). Thickness measurements at each location are reported on isopach maps for the cumulative pumice fallout phases A+C+E+G (Fig. 6a), the pumice fallout phase A (Fig. 6b), the cumulative pyroclastic density current phases B+D+F (Fig. 6c), and the cumulative pumice fallout phases C+E+G (Fig. 6d). These maps are later used to calculate the total grain-size distribution of unit A (see section 4.6), and the volume of deposits (see section 5.1).

The cumulative isopach map of the pumice fallout phases A+C+E+G shows ellipsoidal contour patterns indicating fallout dispersion towards the southwest (Fig. 6a). We find a similar direction of dispersion for the pumice fallout phase A, and the cumulative pumice fallout phases C+E+G (Fig. 6b, d). This direction of dispersion is in relatively good

agreement with the results of Traineau et al. (1989) and Wright et al. (2016) (Fig. 1), and is characteristic of the wind profiles in the Lesser Antilles during the wet season (Michaud-Dubuy et al., 2019). In the upwind direction to the northeast and in the crosswind direction to the southeast, the entire P3 succession is reduced to a single layer of clast-supported, white, angular, fine pumice lapilli containing abundant juvenile and accidental lithic fragments, making it difficult to distinguish the pumice fallout units A, C, E, and G. At locations near the vent, unit A is however clearly visible under the cumulative pumice fallout of units C+E+G (Fig. 4d), which allows to build an individual isopach map for the pumice fallout phase A (Fig. 6b). We note that the northwestern arms of our isopach maps are not well constrained due to a lack of outcrops (in our study as in previous ones) in a region extremely difficult to access due to the presence of dense tropical forest on steep hills.

Units B, D, and F are widespread on the southwest flank of Mt Pelée volcano and the low-concentration PDC deposits almost reached the sea there (Fig. 6c). The high-concentration PDC deposits are channelized in paleo-valleys and now form large plateaux in the Grande Savane, Habitation Depaz and Ajoupa Bouillon areas (see locations in Fig. 1a), an observation consistent with the results of Westercamp and Traineau (1983) and Traineau et al. (1989). However, contrary to Wright et al. (2016), we found no evidence of high-concentration PDC deposits in the Bijou River, Grande River, and Fond Canonville areas (see locations in Fig. 1b).

4.5. Isopleth maps of air fall deposits

Fig. 7 shows the isopleth maps built from the measurements of the major axes of the five largest fragments found at the base and top of unit A, and at the base of unit C. The isopleth map of the base of unit A is well constrained thanks to the good preservation of the deposit (Fig. 7a). However, isopleth contours for the top of unit A and the base of unit C are

411 constrained by only a few points from localities where the two units are separated by the
412 presence of unit B and/or by clear variation in grain-size characteristics (Fig. 7b, c). Isopleth
413 maps for units E and G could not be constructed due to the poor preservation of these
414 deposits. However, in both cases, we were able to draw a single isopleth curve (i.e., the 15
415 mm-isopleth for unit E and 25 mm-isopleth for unit G) that is not reported in Fig. 7. The main
416 direction of dispersion to the southwest (Fig. 7) is consistent with the one inferred from our
417 isopach maps (Fig. 6). Isopleth contours of the top of unit A are clearly more extended in the
418 crosswind direction than those of the base of units A and C.
419
420 4.6. Total grain-size distribution (*Unit A*)
421 We calculated the total grain-size distribution (TGSD) of unit A using the method of
422 Kaminski and Jaupart (1998) (see section 3.3 for calculation details). The interbedded nature
423 and important erosion of the subsequent units made the reconstruction of the TGSD for units
424 B to G impossible. The TGSD of unit A is bimodal with a primary fine mode at 2ϕ and a
425 secondary coarse mode at -2ϕ (Supplementary material Figure S1). The median diameter and
426 sorting for the TGSD of unit A are -0.2ϕ and 2.3, respectively. The amounts of ash (< 2 □□)
427 and fine ash particles (< 63 μm) reach 59 wt.% and less than 1 wt.%, respectively. The latter
428 value should be taken with caution because most of the fine ash particles settled at sea and
429 cannot be taken into account in our grain-size analyses. From these results, we infer that the
430 power law coefficient *D* that fully characterizes the TGSD at the beginning of the P3 eruption
431 (i.e., unit A) is $D = 3.3 \pm 0.1$ (Supplementary material Figure S1). The time evolution of the
432 value of *D* after the phase A remains unknown, but this lack of information will not affect our
433 calculations of the stable plume / collapsing fountain transition that occurred at the end of
434 phase A (see section 6.3).
435

5. Eruptive dynamics

5.1. Erupted volumes

The estimates of volume of tephra fall from phase A using the three integration techniques introduced in section 3 give 0.282 km^3 with the exponential method, 0.316 km^3 with the power law, and 0.306 km^3 with the Weibull function (Fig. 8a). Integration of the exponential, power-law, and Weibull fits for the cumulative pumice fallout C+E+G yields volumes of 0.334, 0.317, and 0.355 km^3, respectively (Fig. 8b). Because the latter estimates are based on three proximal isopach contours only they remain relatively poorly constrained (Fig. 6d). We thus calculated the volume of the cumulative pumice fallout A+C+E+G in order to achieve a better estimate of the total volume of tephra fall. Integrating the exponential, power-law, and Weibull fits yields 0.735, 0.692, and 0.712 km^3, respectively (Fig. 8c). We thus retain a minimum volume of 0.30 ± 0.01 km^3 for unit A, and 0.41 ± 0.02 km^3 for the cumulative pumice fall units C+E+G, and 0.71 ± 0.02 km^3 for the total volume of tephra fall. Based on fallout deposit and magma densities of 1,000 and 2,400 kg m^{-3}, respectively (Traineau et al., 1989), we infer the cumulative DRE volume of fall units to be 0.3 km^3.

The volume of PDC deposits is calculated using the area covered by the dense and dilute PDC deposits. The deposits corresponding to the dilute PDC of phases B, D, and F cover 42, 20, and 36 km^2, respectively (Fig. 6c), which yield bulk volumes of 0.025 km^3 for unit B, 0.010 km^3 for unit D, and 0.016 km^3 for unit G (Calder et al., 1999). The cumulative dense PDC deposits of the phases B, D, and F cover 7 km^2 in Grande Savane, 9.5 km^2 in Habitation Depaz, and 18 km^2 in Ajoupa Bouillon (see locations in Fig. 1a), with an average thickness of 15, 30, and 2 m, respectively (Traineau, 1982). This yields a minimum volume of 0.67 ± 0.02 km^3 DRE for the dense PDC deposits, and gives a total volume of (dense + dilute) PDC deposits of 0.72 ± 0.02 km^3 DRE.

460 The final estimate of the total volume of the P3 eruption (units A+B+C+D+E+F+G) is
461 thus 1.02 ± 0.06 km^3 DRE, and the total mass of tephra emitted is estimated to be 2.4 ± 0.1 x
462 10^{12} kg. The P3 eruption thus stands as a VEI 5 event (Newhall and Self, 1984) with a
463 magnitude of 5.4 (Pyle, 2000).
464
465 5.2. Column heights and exit velocities (*airfall units*)
466 The estimates of maximum height using our isopleth maps (Fig. 7) with the model of Carey
467 and Sigurdsson (1986) give 28.3 ± 3.3 km for the base of unit A, 29.7 ± 1.9 km for the top of
468 unit A, and 16.9 ± 0.4 km for the base of unit C. Following the approach of Bonadonna and
469 Costa (2013), a Weibull fit gives a maximum height of 28.1 ± 1 km for the base of unit A,
470 30.0 ± 0.5 km for the top of unit A, and 17.2 ± 0.5 km for the base of unit C (Supplementary
471 material Figure S2). The lack of information about the distribution of lithic sizes in unit E and
472 G prevents us from providing a robust estimate for the maximum height. Based on a single
473 isopleth curve in each case, we calculate maximum column heights of 12 ± 4 km for unit E
474 and 13 ± 4 km for unit G using the model of Carey and Sigurdsson (1986).
475 We also use data on the decrease of lithic sizes with distance from the vent in
476 Supplementary material Figure S2 to estimate the minimum exit velocity of the volcanic
477 plume at the vent. Extrapolating the Weibull fits down to $A^{1/2}$ = 0.01 km to find the maximum
478 lithic size at the vent, we infer minimum exit velocities of 210 ± 10 m s^{-1} for the base of unit
479 A, 220 ± 10 m s^{-1} for the top of unit A, and 220 ± 10 m s^{-1} for the base of unit C.
480
481 5.3. Mass eruption rates and duration
482 We use our new estimates of maximum column height to calculate the mass eruption rate
483 (MER) feeding the plume during the P3 eruption. The model of Girault et al. (2016) used with
484 their complex wind profile, which is close to the average wind profiles in the Lesser Antilles,

485 yields maximum MERs of 10^8 kg s^{-1} for the beginning of phase A, 1.5 x 10^8 kg s^{-1} for the end
486 of phase A, 3 x 10^7 kg s^{-1} for phase C, 1.4 x 10^7 kg s^{-1} for phase E, and 1.7 x 10^7 kg s^{-1} for
487 phase G. The empirical formula of Mastin et al. (2009) built on observations of 28 Plinian
488 eruptions yields maximum MERs of 1.4 x 10^8 kg s^{-1} for the beginning of phase A, 1.9 x 10^8
489 kg s^{-1} for the end of phase A, 1.8 x 10^7 kg s^{-1} for phase C, 4.2 x 10^6 kg s^{-1} for phase E, and 5.9
490 x 10^6 kg s^{-1} for phase G. Based on these two series of estimates, we retain peak MERs of 1.2
491 ± 0.2 x 10^8 kg s^{-1} for the beginning of phase A, 1.7 ± 0.2 x 10^8 kg s^{-1} for the end of phase A,
492 2.4 ± 0.6 x 10^7 kg s^{-1} for phase C, 9.1 ± 4.9 x 10^6 kg s^{-1} for phase E, and 1.2 ± 0.5 x 10^7 kg s^{-1}
493 for phase G. Combined with masses of fallout deposits (section 5.1), these MER provide
494 minimum durations of ~45 min for phase A, ~1h45 for phase C, ~3h for phase E, and ~2h45
495 for phase G.

496 The MER during the collapsing phases B, D, and F is more difficult to assess. The
497 model of Bursik and Woods (1996) yields a mass eruption rate of ~ 2.3 ± 0.8 x 10^8 kg s^{-1} for
498 the three phases B, D, and F. We note that this value does not take into account topographic
499 slopes but Doyle et al. (2010) showed that the runout distance of such a flow mostly depends
500 on the initial collapse height, which is imposed by the MER rather than by ground slopes.
501 Combined with masses of PDC deposits (section 5.1), this MER provides minimum durations
502 of ~50 min for phase B, ~25 min for phase D, and ~50 min for phase F.

503

504 **6. Discussion**

505 Our revisit of the P3 deposits shows that the eruption started with the formation of a stable
506 column that spread pyroclasts to the southwest of the volcano (phase A). This initial phase
507 was immediately followed by a partial collapse of the column producing alternating tephra
508 fallout (phases C, E, G) and pyroclastic density currents (phases B, D, E). We now compare
509 our results to previous work on the P3 eruption, and on the younger P1 and P2 eruptions of

510 Mt Pelée volcano. We then focus our discussion on the causes of partial column collapse
511 during the P3 eruption by using a physical model of volcanic plumes.
512
513 6.1 Comparison with previous studies of P3 eruption
514 Our new stratigraphic data regarding the P3 succession largely differs from those of previous
515 studies (Westercamp and Traineau, 1983; Traineau et al., 1989; Wright et al., 2016). The $P3_1$
516 phase identified by Westercamp and Traineau (1983) corresponds to our eruptive unit A, and
517 their $P3_3$ phase most likely corresponds to our entire sequence from unit B to unit G. The
518 distal products identified by Wright et al. (2016) were attributed to the P3 eruption based on a
519 single radiocarbon age determined from a charcoal sampled at the top of their stratigraphic
520 section (see their figure 6). We revisited their outcrop locations 2 and 3 along a main road,
521 and found that their stratigraphic section lies beneath the 13.5 ka cal BP Bellefontaine Plinian
522 eruption (Michaud-Dubuy et al., 2019). To further reinforce our observation, we sampled a
523 paleosol at the base of their stratigraphic section and obtained a radiocarbon age of 17,750 ±
524 100 yr BP, which indicates that the distal deposits studied by Wright et al. (2016) are much
525 older than the P3 eruption.
526 The total volume of the P3 eruption (units A+B+C+D+E+F+G) is calculated to be
527 1.02 ± 0.06 km^3 DRE, which is one order of magnitude larger than the 0.19 km^3 DRE
528 previously estimated (Traineau et al., 1989). We attribute this important discrepancy to the
529 large volume of PDC deposits that were not taken into account in Traineau et al. (1989), and
530 to the improvement of the reconstruction techniques used here to calculate the total volume of
531 a pumice fall deposit (Bonadonna and Costa, 2013). The maximum column height is
532 estimated to be ~ 30 km at the end of phase A, which is much higher than the previous
533 estimates (> 6 km by Traineau et al., 1989 and < 12 km by Wright et al., 2016). Again we
534 attribute this important difference to the better quality of our isopleth maps and to the

535 improvement of the reconstruction techniques used to estimate the maximum height from the
536 distribution of lithic fragments in the field.
537
538 6.2 Comparison with younger Plinian eruptions in Martinique (P1 and P2)
539 The three latest Plinian eruptions at Mt Pelée volcano (P1, P2 and P3) have similar
540 depositional successions that can be interpreted to result from the partial collapse of an
541 initially stable Plinian column (Traineau et al., 1989; Carazzo et al., 2012, 2019; Wright et al.,
542 2016). The total DRE volume estimated for P3 (~1 km^3) is larger than those of the P1 (~0.2
543 km^3) and P2 (~0.8 km^3) eruptions. The maximum column height during the phase of sustained
544 Plinian column is also larger for P3 (28-30 km) than for the P1 (19-22 km) and P2 (22-26 km)
545 eruptions. Consequently, the mass eruption rate is estimated to be larger for P3 (1.4 x 10^8 kg
546 s^{-1}) than for P1 (3.6 x 10^7 kg s^{-1}) and P2 (1.1 x 10^8 kg s^{-1}). The minimum eruption durations
547 are 11h for P3, 7h for P2, and 5h for P1. The total grain-size distribution is however relatively
548 similar for the three events, with power law exponent *D* of 3.3, 3.4-3.5, and 3.2-3.3 for P3,
549 P2, and P1, respectively. Our estimates of exsolved gas contents for P3 (2-2.9 wt.% - see
550 section 6.3 for calculations details) are larger than those of P1 (1.6-2.1 wt.%) and P2 (1.7-2.1
551 wt.%). The minimum exit velocities inferred from the distribution of lithic fragments for P3
552 (210-220 m s^{-1}) are also larger than those of P1 (150-165 m s^{-1}) and P2 (180-200 m s^{-1}), a
553 result consistent with our estimates of free gas contents. Table 2 summarizes the eruptive
554 parameters retrieved for the last three Plinian eruptions at Mt Pelée volcano. P3 stands as a
555 large Plinian eruption more powerful and voluminous (VEI 5, M 5.4) than the P1 (VEI 4, M
556 4.6) and P2 (VEI 4, M 5.2) eruptions. However, because these three eruptions have much in
557 common, in particular similar pre-eruptive conditions (Martel et al., 1998; Martel and
558 Poussineau, 2007), they can be used to test the performance of theoretical models in
559 predicting the conditions for column collapse.

560

561 6.3 The stable plume / pyroclastic fountain transition during a sustained Plinian eruption

562 The P3 eruption underwent partial column collapse after an initial phase of stable Plinian
563 plume. Wilson et al. (1980) showed that the mass eruption rate and the amount of free gas in
564 the volcanic mixture at the vent both strongly control the transition between the stable Plinian
565 plume and the collapsing fountain regimes. Our estimates of the MER show a progressive
566 increase over time from ~1.2 x 10^8 kg s^{-1} (base of unit A) to ~2.5 x 10^8 kg s^{-1} (unit B+C) (Fig.
567 9), an evolution consistent with the increase in maximum lithic sizes throughout unit A (Fig.
568 3c). Other powerful eruptions underwent a similar evolution leading to column collapse, such
569 as the 79 CE Vesuvius (Shea et al., 2011), and the 186 CE Taupo (Walker, 1980) eruptions.

570 The time evolution of total gas content feeding the column at the vent is more difficult
571 to assess. Petro-geochemical measurements provide quantitative estimates of pre-eruptive
572 magma storage conditions, including temperature (875-900°C), pressure (~200 ± 50 MPa),
573 and water content (~5.8 ± 0.5 wt.%) (Martel et al., 1998; Martel and Poussineau, 2007). Here,
574 we use the magmatic water content measured in glass inclusions available in the literature as a
575 total volatile content in the melt (n_0). Correcting this value from the presence of crystals and
576 lithic fragments (Table 3), we find that the initial gas content (x_0) in the magma decreased
577 from 4.1 to 2.9 wt.% during the eruption (Table 3). As in Kaminski and Jaupart (1998) and
578 Carazzo et al. (2012; 2019), we calculate the mass fraction of exsolved gas in the mixture at
579 fragmentation level (x_f) for a threshold vesicularity of 70 %, which assumes closed-system
580 conditions consistent with degassing models built on U-series measurements in the P3
581 eruption products (Villemant et al., 1996). We find that x_f decreases from 2.9 to 2.1 wt.%
582 during the eruption (Fig. 9). To strengthen these estimates, we calculate the theoretical exit
583 velocities at the vent assuming that the volcanic mixture decompresses freely into the
584 atmosphere (Woods and Bower, 1995). For this, we infer the effective amount of free gas in

585 the volcanic mixture at the base of the column that is modulated by gas entrapment by
586 pumices as a function of their size distribution (Kaminski and Jaupart, 1998). We use the
587 power law exponent D = 3.3 (for unit A) estimated in section 4.6, and a typical open porosity
588 of 60-70 % (Michaud-Dubuy et al., 2018) to calculate an amount of free gas of 2.4-2.7 wt.%
589 for phase A. These estimates provide exit velocities after decompression in the range 215-230
590 m s^{-1} (Table 3) that are consistent with those estimated from the distribution of the lithic
591 fragments collected at the base and top of unit A (see section 5.2). This relatively good
592 agreement at least for phase A reinforces the confidence that our estimates of x_f provide
593 reasonable values of free gas content during the P3 eruption.
594 Fig. 10 compares the estimated values of MER and exsolved gas content in the column
595 at collapse with the theoretical 1D predictions for tropical conditions (Michaud-Dubuy et al.,
596 2018). The conditions at the beginning of the P3 eruption formed a stable plume as predicted
597 by the model. During phase A, the combined effect of a slightly increasing MER and a
598 decreasing gas content led the eruption to conditions close to the plume/fountain transition.
599 The eruption reached a peak in MER during the concomitant phases B and C, which most
600 likely induced the partial column collapse. During the partial column collapse stage of the
601 eruption (units B to G), the MER did not change significantly but the gas content slowly
602 decreased until the end of the eruption. The fairly good agreement between our field data and
603 the theoretical model can be taken as an indirect confirmation of the proposed evolution of the
604 total gas content feeding the column, even if a direct confirmation is not possible.
605 Furthermore, our results suggest that the stable column underwent partial collapse soon after
606 the beginning of the eruption (i.e., within less than a hour), an evolution that was also inferred
607 from the analysis of the P1 and P2 Plinian eruption deposits (Carazzo et al., 2012; 2019). In
608 these three eruptions, the transition occurred at conditions well predicted by our theoretical
609 model of volcanic plumes (Fig. 10).

610 Comparing these results with other historical eruptions requires gathering well-
611 constrained values of exsolved gas contents, mass eruption rates and power-law exponent *D*
612 of the TGSD (Michaud-Dubuy et al., 2018). There are however only a few examples of such
613 well-documented events, and we choose here to compare our results to the 186 CE Taupo
614 (VEI 7) and 79 CE Vesuvius (VEI 5) eruptions. Fig. 10 shows that the model successfully
615 predicts the transition for the Taupo eruption but fails to explain the transition for the
616 Vesuvius eruption. Furthermore, one can note that the collapsing phase of the 79 CE Vesuvius
617 eruption is characterized by the same amount of gas and MER at the source as the stable
618 phase (end of phase A) of the P3 eruption. The only difference between the two cases is the
619 total grain-size distribution. Indeed, as discussed in Michaud-Dubuy et al. (2018), the 79 CE
620 Vesuvius eruption is characterized by a specific total grain-size distribution (D = 3.0) where
621 pyroclasts are in average not large enough to be lost by sedimentation but not small enough to
622 be in thermal equilibrium with the gas. The hypothesis of thermal equilibrium between the
623 gas and pyroclasts that is used in our 1D model of volcanic plumes, valid for the fine grain-
624 size distribution of the beginning of the P3 eruption (D = 3.3), may therefore not hold
625 anymore for this eruption and may explain the peculiar collapse conditions.
626
627 **7. Conclusion**
628 We have presented a new comprehensive field study of the P3 eruption, and a detailed
629 reconstruction of the mechanisms controlling the eruptive dynamics. New radiocarbon
630 measurements, averaged with those previously available, provide a refined age of 79 ± 21 cal
631 CE for this event. The eruption started with the formation of a 28 to 30 km-high stable
632 column (phase A), which partially collapsed due to the combined effect of increasing MER
633 and decreasing gas content (phase B). In the partial collapse regime, the eruptive mixture
634 formed a 12 to 17 km-high marginally stable column (phases C, E, and G) punctuated with

635 the production of PDC fed by the partially collapsing column (phases B, D, and F). Our
636 calculations show that P3 was a large Plinian eruption (VEI 5, M = 5.4) evolving close to the
637 plume/fountain transition. The total volume of tephra reached 1 km^3 DRE, and the mass
638 eruption rate was of the order of 10^8 kg s^{-1} during a period of at least 11h.

639 The P3 eruption is more powerful than the last two Plinian eruptions in Martinique but
640 the three eruptions underwent similar evolution towards a marginally stable volcanic column.
641 This recurrent phenomenon provides a great opportunity to look carefully at the parameters
642 affecting column stability, to constrain theoretical models of volcanic plumes, and thus
643 improve volcanic disaster forecasting. Petrological and geochemical measurements on the P3
644 eruptive products may help to further investigate the complexity of magma degassing,
645 crystallization and fragmentation in the volcanic conduit (Gurioli et al., 2005; Martel and
646 Poussineau, 2007; Shea et al., 2012; 2014), and thus refine the estimated values of exsolved
647 gas content at the vent. The global consistency between our theoretical predictions and field
648 observations of column collapse for a number of Plinian eruptions confirms that current
649 theoretical 1D models of volcanic plumes predict correctly the conditions of collapse when
650 the total grain-size distribution is dominated by fine fragments (i.e., obeys a power law
651 distribution with an exponent strictly larger than 3). Our results can thus be used to assess the
652 dominant hazard during a Plinian scale event, which may pass from pumice fall to PDC as
653 eruptive conditions vary.

654 Mt Pelée volcano is currently quiescent but the reconstruction of its eruptive history
655 over the past 5,000 years shows that a Plinian eruption is a major potential scenario in the
656 future. Such an event with the magnitude of the P3 eruption would disrupt the lives of more
657 than 376,000 people living in Martinique and possibly impact other volcanic islands
658 depending on the wind speed and direction.

659

Acknowledgements

We warmly thank the staff of the Mt Pelée volcanological observatory (OVSM) for field and administrative assistance, J.-P. Dumoulin, L. Beck, E. Delque-Kolic and C. Moreau (LMC14, CNRS UMS2572) who performed the ^{14}C dating, G. Delaviel-Anger and T. Crouzal for their help in the field, and A. Jegouzo for enthusiastic discussions about the P3 eruption. This work was partially funded by the Institut National des Sciences de l'Univers – Centre National de la Recherche Scientifique progamme CT3-ALEA, INSU-CNRS Artemis 2016 and 2017 for ^{14}C dating, and CASAVA (ANR contract ANR-09-ANR-RISK-002) and RAVEX (ANR contract ANR-16-CE03-0002). This study contributes to the IdEx project "Université de Paris" (ANR-18-IDEX-0001).

References

Bardintzeff, J.M., Miskovsky, J.-C., Traineau, H., Westercamp, D., 1989. The recent pumice eruptions of Mt Pelée, Martinique. Part II: Grain-size studies and modelling the last Plinian phase P1. J. Volcanol. Geotherm. Res. 38: 35-48.

Bonadonna, C., Costa, A. 2012. Estimating the volume of tephra deposits: a new simple strategy. Geology 40(5): 415-418.

Bonadonna, C., Costa, A., 2013. Plume height, volume, and classification of explosive volcanic eruptions based on the Weibull function. Bull. Volcanol. 75: 742-761.

Bonadonna, C., Houghton, B.F., 2005. Total grain-size distribution and volume of tephra fall deposits. Bull. Volcanol. 67: 441-456.

Branney, M.J., Kokelaar, B.P., 2002. Pyroclastic density currents and the sedimentation of ignimbrites. Geol. Soc. Mem. 27, 143 p.

Bronk Ramsey, C., 2009. Bayesian analysis of radiocarbon dates. Radiocarbon 51: 337–360.

Bursik, M.I., Woods, A.W., 1996. The dynamics and thermodynamics of large ash flows. Bull. Volcanol. 58: 175– 193.

Calder, E.S., Cole, P.D., Dade, W.B., Druitt, T.H., Hoblitt, R.P., Huppert, H.E., Ritchie, L., Sparks, R.S.J., Young, S.R., 1999. Mobility of pyroclastic flows and surges at the Soufriere Hills Volcano, Montserrat. Geophys. Res. Lett. 26: 537–540.

Carazzo, G., Tait, S., Kaminski, E., Gardner, J.E., 2012. The recent Plinian explosive activity of Mt. Pelée volcano (Lesser Antilles): The P1 AD 1300 eruption, Bull. Volcanol. 74: 2187-2203.

Carazzo, G., Kaminski, E., Tait S., 2015. The timing and intensity of column collapse during explosive volcanic eruptions. Earth Planet. Sci. Lett. 411: 208-217.

Carazzo, G., Tait, S., Kaminski, E., 2019. Marginally stable recent plinian eruptions of Mt. Pelée volcano (Lesser Antilles): The P2 AD 280 eruption, Bull. Volcanol. 81: 1-17.

706 Carey, S., Sigurdsson, H., 1986. The 1982 eruptions of El Chichon volcano, Mexico (2):
707 Observations and numerical modelling of tephra-fall distribution. Bull. Volcanol. 48: 127-
708 141.
709
710 Dade, W.B., Huppert, H.E., 1998. Long runout rockfalls. Geology 26: 803-806.
711
712 Daggit, M.L., Mather, T.A., Pyle, D.M., Page, S., 2014. AshCalc – a new tool for the
713 comparison of the exponential, power-law and Weibull models of tephra deposition. J. Appl.
714 Volcanol. 3: 7.
715
716 Di Muro, A., Neri, A., Rosi, M., 2004. Contemporaneous convective and collapsing eruptive
717 dynamics: the transitional regime of explosive eruptions. Geophys. Res. Lett. 31: L10607.
718
719 Di Muro, A., Rosi, M., Aguilera, E., Barbieri, R., Massa, G., Mundula, F., Pieri, F., 2008.
720 Transport and sedimentation dynamics of transitional explosive eruption columns: the
721 example of the 800 BP Quilotoa eruption (Ecuador). J. Volcanol. Geotherm. Res. 174: 307-
722 324.
723
724 Doyle, E.E., Hogg, A.J., Mader, H.M., Sparks, R.S.J., 2010. A two-layer model for the
725 evolution and propagation of dense and dilute regions of pyroclastic currents. J. Volcanol.
726 Geotherm. Res. 190: 365–378.
727
728 Fierstein, J., Hildreth, W., 1992. The Plinian eruptions of 1912 at Novarupta, Katmai National
729 Park, Alaska. Bull. Volcanol. 54: 646-684.
730

731 Girault, F., Carazzo, G., Tait, S., Ferrucci, F., Kaminski, E., 2014. The effects of total grain-
732 size distribution on the dynamics of turbulent volcanic plumes. Earth Plan. Sci. Lett. 394:
733 124-134.
734
735 Girault, F., Carazzo, G., Tait, S., Kaminski, E., 2016. Combined effects of total grain-size
736 distribution and crosswind on the rise of explosive volcanic columns. J. Volcanol. Geotherm.
737 Res. 326: 103-113.
738
739 Gurioli, L., Houghton, B.F., Chasman, K.V., Cioni, R., 2005. Complex changes in eruption
740 dynamics during the 79 AD eruption of Vesuvius. Bull. Volcanol. 67; 144-159.
741
742 Kaminski, E., Jaupart, C., 1998. The size distribution of pyroclasts and the fragmentation
743 sequence in explosive volcanic eruptions. J. Geophys. Res. 103: 29,759-29,779.
744
745 Koyaguchi, T., Tokuno, M., 1993. Origin of the giant eruption cloud of Pinatubo, June 15,
746 1991. J. Volcanol. Geotherm. Res. 55: 85-96.
747
748 Mastin, L.G., Guffanti, M., Sezrvranckx, R., Webley, P., Barsotti, S., dean, K., Durant, A.,
749 Ewert, J.W., Neri, A., Rose, W.I., Schneider, D., Siebert, L., Stunder, B., Swanson, G.,
750 Tupper, A., Volentik, A., Waythomas, C.F., 2009. A multidisciplinary effort to assign
751 realistic source parameters to models of volcanic ash-cloud transport and dispersion during
752 eruptions. J. Volcanol. Geotherm. Res. 186: 10-21.
753
754 Martel, C., Pichavant, M., Bourdier, J.-L., Traineau, H., Holtz, F., Scaillet, B., 1998. Magma

storage conditions and control of eruption regime in silicic volcanoes: experimental evidence from Mt Pelée. Earth Planet. Sci. Lett. 156: 89–99.

Martel, C., Poussineau, S., 2007. Diversity of eruptive styles inferred from the microlites of Mt. Pelée andesite (Martinique, Lesser Antilles). J. Volcanol. Geotherm. Res. 166: 233–254.

Michaud-Dubuy, A., Carazzo, G., Kaminski, E., Girault, F., 2018. A revisit of the role of gas entrapment on the stability conditions of explosive volcanic columns. J. Volcanol. Geotherm. Res. 357: 349-361.

Michaud-Dubuy, A., Carazzo, G., Tait, S., Le Hir, G., Fluteau, F., Kaminski, E., 2019. Impact of wind direction variability on hazard assessment in Martinique (Lesser Antilles): the example of the 13.5 ka cal BP Bellefontaine Plinian eruption of Mount Pelée volcano. J. Volcanol. Geotherm. Res. 381: 193-208.

Newhall, C.G., Self., S., 1982. The volcanic explosivity index (VEI): an estimate of explosive magnitude for historical volcanism. J. Geophys. Res. 87: 1231-1238.

Pyle, D.M., 1989. The thickness, volume and grainsize of tephra fall deposits. Bull. Volcanol. 51:1–15.

Pyle, D.M., 2000. Sizes of volcanic eruptions. In: Sigurdsson, H., Houghton, B., Reimer, H., Stix, J., McNutt, S. (eds) Encyclopedia of volcanoes. Academic, San Diego, pp 263-269.

779 Reimer, P., 2013. Selection and treatment of data for radiocarbon calibration: an update to the
780 international calibration (IntCal) criteria. Radiocarbon 55: 1923–1945.
781
782 Roobol M.J., Smith A.L., 1976. Stratigraphic studies of Mount Pelée, Martinique. Bull.
783 B.R.G.M., sect. IV, 4: 297–304.
784
785 Self, S., Rampino, M.R., 2012. The 1963-1964 eruption of Agung volcano (Bali, Indonesia).
786 Bull. Volcanol. 74: 1521-1536.
787
788 Shea, T., Gurioli, L., Houghton, B.F., Cioni, R., Cashman, K.V., 2011. Column collapse and
789 generation of pyroclastic density currents during the A.D. 79 eruption of Vesuvius: The role
790 of pyroclast density. Geology 39: 695-698.
791
792 Shea, T., Gurioli, L., Houghton, B.F., 2012. Transitions between fall phases and pyroclastic
793 density currents during the AD 79 eruption at Vesuvius: Building a transient conduit model
794 from the textural and volatile record. Bull. Volcanol. 74: 2363-2381.
795
796 Shea, T., Hellerbrand, E., Gurioli, L., Tuffen, H., 2014. Conduit- to localized-scale degassing
797 during Plinian eruptions: Insights from major element and volatile (Cl and H_20) analyses
798 within Vesuvius AD 79 pumice. J. Petrol. 55(2): 315-344.
799
800 Sigurdsson, H., Carey, S., Fisher, R.V., 1984. The 1982 eruptions of El Chichon volcano,
801 Mexico: stratigraphy of pyroclastic deposits. J. Volcanol. Geotherm. Res. 23: 11-37.
802

803 Suzuki, Y.J., Costa, A., Cerminara, M., Esposti Ongaro, T., Herzog, M., Van Eaton, A.R.,
804 Denby, L.C., 2016. Inter-comparison of three dimensional models of volcanic plumes. J.
805 Volcanol. Geotherm. Res. 326: 26-42.
806
807 Traineau, H., 1982. Contribution à l'étude géologique de la Montagne Pelée, Martinique.
808 Evolution de l'activité éruptive au cours de la période récente. Thèse de 3ième cycle,
809 Université de Paris Sud, Orsay, 209 p.
810
811 Traineau, H., Westercamp, D., Bardintzeff, J.M., Miskovsky, J.C., 1989. The recent pumice
812 eruptions of Mt. Pelée volcano, Martinique. Part I: Depositional sequences, description of
813 pumiceous deposits. J. Volcanol. Geotherm. Res. 38: 17–33.
814
815 Turcotte, D.L., 1986. Fractals and fragmentation. J. Geophys. Res. 91: 1921-1926.
816
817 Villemant, B., Boudon, G., Komorowski J.-C., 1996. U-series disequilibrium in arc magmas
818 induced by water-magma interaction. Earth Planet. Sci. Lett. 140: 259-267.
819
820 Walker, G.P.L., 1980. The Taupo pumice: product of the most powerful known (ultraplinian)
821 eruption? J. Volcanol. Geotherm. Res. 8: 69-94.
822
823 Walker, G.P.L., 1983. Explosive volcanic eruptions - a new classification scheme. Geol.
824 Rundsch. 62: 431-446.
825
826 Ward, G.K., Wilson, S.R., 1978. Procedures for comparing and combining radiocarbon age
827 determinations: a critique. Archaeometry 20: 19–31.

828

829 Westercamp D., Traineau H., 1983. The past 5,000 years of volcanic activity at Mt. Pelée
830 Martinique (F.W.I.): implications for assessment of volcanic hazards. J. Volcanol. Geotherm.
831 Res. 17: 159–185.
832
833 Wilson, L., Sparks, R.S.J., Walker, G.P.L., 1980. Explosive volcanic eruptions-IV. The
834 control of magma properties and conduit geometry on eruption column behavior. Geophys. J.
835 R. Astron. Soc. 63: 117-148.
836
837 Wilson, L., Walker, G.P.L., 1985. The Taupo eruption, New Zealand. I General aspects.
838 Philos. Trans. R. Soc. Lond. A 314: 199-228.
839
840 Wilson, G., Wilson, T.W., Deligne, N.I., Cole, J.W., 2014. Volcanic hazard impacts to critical
841 infrastructure: a review. J. Volcanol. Geotherm. Res. 286: 148-182.
842
843 Woods, A.W., Bower, S.M., 1995. The decompression of volcanic jets in a crater during
844 explosive volcanic eruptions. Earth Planet. Sci. Lett. 131: 189-205.
845
846 Wright, J.V., Smith A.L., Roobol M.J., Mattioli G.S., Fryxell J.E., 2016. Distal ash hurricane
847 (pyroclastic density current) deposits from a ca. 2000 yr B.P. Plinian-style eruption of Mount
848 Pelée, Martinique: Distribution, grain-size characteristics, and implications for future hazards,
849 Geol. Soc. Am. Bull. 128: 777–791.
850

851 **Table captions**

852

Sample	Site	Unit	Subunit	Altitude (m)	Distance from the vent (km)	Thickness (cm)
1	163	A	(0-40 cm)	269	3.7	160
2	163	A	(40-60 cm)	269	3.7	160
3	163	A	(60-100 cm)	269	3.7	160
4	163	A	(100-140 cm)	269	3.7	160
5	163	A	(140-160 cm)	269	3.7	160
6	163	B	Bulk	269	3.7	18
7	163	C	Bulk	269	3.7	20
8	163	D	Bulk	269	3.7	15
9	163	E	Bulk	269	3.7	13
10	163	F	Bulk	269	3.7	6
11	163	G	Bulk	269	3.7	37
12	88	A-G	Bulk	466	4.3	45
13	66b	A-G	Bulk	371	4.9	65
14	142	A-G	Bulk	234	5.8	60
15	194	A-G	Bulk	280	5.8	55
16	114	A-G	Bulk	195	6.3	105
17	137	A-G	Bulk	19	6.5	100
18	191	A-G	Bulk	35	6.5	46
19	144	A-G	Bulk	47	6.6	80
20	145	A-G	Bulk	540	11.9	25

853 **Table 1**: Sampling of the P3 deposits for grain-size analysis.

854

855

856

857

858

859

860

861

862

863

864

Parameters	**P3 (79 CE)**	**P2 (280 CE)**	**P1 (1300 CE)**
Total DRE volume	**1.02 km^3**	0.77 km^3	0.16 km^3
Erupted mass	**2.4 x 10^{12} kg**	1.7 x 10^{12} kg	4 x 10^{11} kg
VEI	**5**	4	4
Magnitude	**5.4**	5.2	4.6
Maximum column height	**30 km**	26 km	22 km
Maximum PDC runout	**7 – 10.3 km**	7 – 11.5 km	4.5 – 8 km
Maximum MER (fall)	**1.4 x 10^8 kg s^{-1}**	1.1 x 10^8 kg s^{-1}	3.6 x 10^7 kg s^{-1}
Maximum MER (PDC)	**2.5 x 10^8 kg s^{-1}**	3.1 x 10^8 kg s^{-1}	9 x 10^7 kg s^{-1}
Maximum intensity	**11.4**	11.5	11
Duration	**> 11 h**	> 7 h	> 5 h
TGSD	**D = 3.3**	D = 3.4 - 3.5	D = 3.2 – 3.3
Minimum exit velocity	**210 - 220 m s^{-1}**	180 – 200 m s^{-1}	150 – 165 m s^{-1}
Total gas content	**2 - 2.9 wt.%**	1.8 – 2.2 wt.%	1.6 – 2.1 wt.%

865 **Table 2**: Summary of the estimated eruptive parameters for the P3 eruption, and comparison
866 with P1 and P2 (Carazzo et al., 2012; 2019).
867
868
869
870
871
872
873
874

Phase	n_0 (wt.%)	α_c	x_0 (wt.%)	x_f (wt.%)	U_{free} (m s^{-1})	U_{min} (m s^{-1})
Early A	5.8	29	4.1	2.9	230	210
Late A	5.8	38	3.6	2.5	215	220
B-C	5.8	42	3.4	2.3	-	220
D-E	5.8	45	3.2	2.2	-	-
F-G	5.8	49	2.9	2.1	-	-

Table 3: Gas contents and deduced exit velocities. n_0 is the total volatile content of the melt (Martel et al., 1998), α_c is the percentage of crystals in the melt plus lithics in the flow, x_0 is the mass fraction of gas in the magma assuming complete degassing, x_f is the mass fraction of exsolved gas in the gas+pyroclasts mixture at fragmentation for a threshold vesicularity of 70%, U_{free} is the supersonic velocity after decompression calculated using x_0, D = 3.3 and an open porosity of 60-70% (Michaud-Dubuy et al., 2018), and U_{min} is the eruptive velocity deduced from the distribution of the lithic fragments (section 5.2).

893 **Figure captions**

894

895 **Fig. 1**: Current maps for the P3 eruption. **a** Isopach map (in centimeters) from Westercamp
896 and Traineau (1983). (1) Dashed and (2) dotted lines correspond to isopachs for the pumice
897 fallout deposit $P3_1$ and $P3_2$, respectively. (3) The light grey and (4) dark areas give the
898 distribution of the low-concentration PDC (surge), and high-concentration PDC (flow)
899 deposits $P3_3$, respectively. **b** Isopach map (in centimeters) from Wright et al. (2016). (1)
900 Dashed lines correspond to isopachs for a pumice fallout deposit. (2) The light and (3) dark
901 grey areas give the distribution of a low-concentration PDC (surge) deposit, and a low-
902 concentration PDC (ash hurricane) deposit, respectively. (4) The dark areas correspond to
903 high-concentration PDC (flow) deposits.

904

905 **Fig. 2**: Overview of our field area in Martinique (inset). White circles and numbers refer to
906 localities where P3 deposits are present. Black dots show outcrops where P3 deposits are
907 absent (due to erosion) and/or too deeply buried under recent eruption deposits. The dotted
908 lines give the stratigraphic correlation reported in Fig. 5.

909

910 **Fig. 3**: **a** Composite stratigraphic section showing typical unit thickness and grain-size
911 characteristics of the P3 eruptive sequence. **b** Grain-size distribution selected samples
912 representing the different eruptive units, including five stratigraphic heights in unit A, at
913 location 163. **c** Variations of the median grain-size (blue circles), sorting (green circles),
914 juvenile lithic content (grey squares), accidental lithic content (dark squares), total lithic
915 content (white squares), and lithic size (red squares) along the stratigraphic height at location
916 163.

917

Fig. 4: Representative photographs of outcrops of the P3 deposits in Martinique at sites **a** 57, **b** 78, **c** 13, **d** 65, and **e, f** 163. See Fig. 2 for location and distance from the source. All scale bars are 20 cm long.

Fig. 5: Stratigraphic logs of representative sections of deposits of the P3 eruption. See Fig. 2 for outcrop locations.

Fig. 6: Isopach maps (in centimeters) for **a** the cumulative pumice fallout (units A+C+E+G), **b** the pumice fallout unit A, **c** the cumulative PDC deposits (units B+D+F) and **d** the cumulative pumice fallout (units C+E+G). Open circles indicate measured sample locations. Bold numbers in panel (c) indicate the thicknesses of high-concentration PDC deposits.

Fig. 7: Isopleth maps (in millimeters) for the lithic fragments sampled **a** at the base of unit A, **b** at the top of unit A, and **c** the base of unit C. Open circles indicate measured sample locations. Direction of dispersal axes is consistent with those inferred from the isopach maps.

Fig. 8: Deposit thinning profiles generated from the isopach maps for **a** unit A, **b** the cumulative pumice fallout C+E+G, and **c** the cumulative pumice fallout A+C+E+G represented by semi-log plots of square root of isopach areas (in kilometers) versus thickness (in meters). Thinning trends are approximated by exponential (purple dashed line), power-law (blue dotted line), and Weibull (red solid line) fits.

Fig. 9: Summary of the time evolution of the P3 eruptive parameters. **a** Cumulative erupted mass (in kg). **b** Maximum column height (in km). **c** Mass eruption rate (in kg s^{-1}). **d** Total exsolved gas content, x_f (in wt.%).

Fig. 10: Transition diagram depicting the P3 eruptive events and depositional units (diamonds), and comparison with the P1 (squares), P2 (triangles), Taupo (circles) and Vesuvius (inverted triangles) eruptions. Numbers associated with diamonds correspond to different phases of the P3 eruption: 1: beginning of phase A, 2: end of phase A, 3: simultaneous phases B and C, 4: simultaneous phases D and E, and 5: simultaneous phases F and G. Dashed line corresponds to the maximum mass eruption rate feeding the column before collapse as a function of the total gas content at the column base (using Michaud-Dubuy et al. (2018) model for tropical conditions and $D = 3.3$). Open, gray, and dark symbols correspond to geological data inferred for the stable column phase, partial column collapse phase, and total column collapse phase, respectively. Data for the P1, P2, Taupo and Vesuvius eruptions are compiled in Carazzo et al. (2012, 2019) and Michaud-Dubuy et al. (2018), respectively.

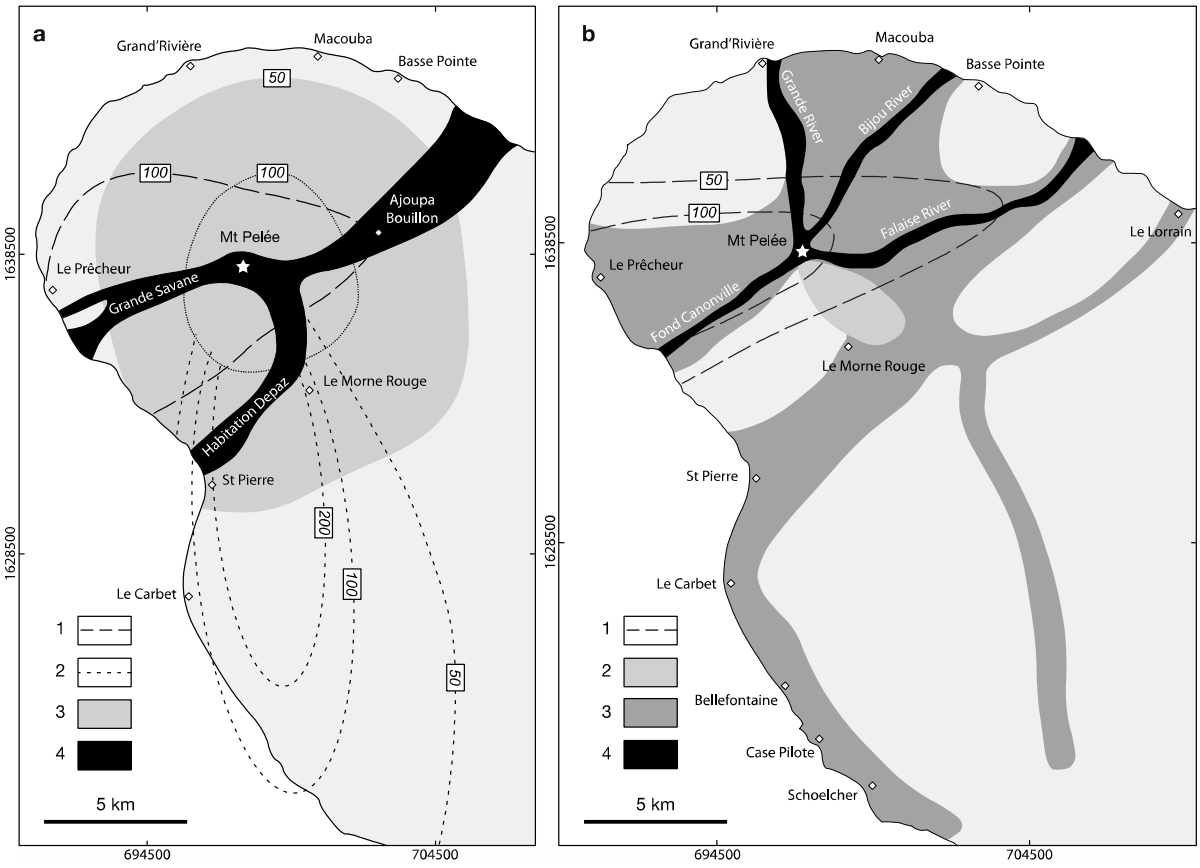
a
Grand'Rivière
Macouba
Basse Pointe
50
100
100
Ajoupa
Bouillon
Mt Pelée
Le Prêcheur
Grande Savane
Le Morne Rouge
Habitation Depaz
St Pierre
200
100
50
Le Carbet
1
2
3
4
5 km
1638500
1628500
694500
704500
b
Grand'Rivière
Macouba
Basse Pointe
Grande River
Bijou River
50
100
Falaise River
Mt Pelée
Le Lorrain
Le Prêcheur
Fond Canonville
Le Morne Rouge
St Pierre
Le Carbet
1
2
3
4
Bellefontaine
Case Pilote
Schoelcher
5 km
1638500
1628500
694500
704500

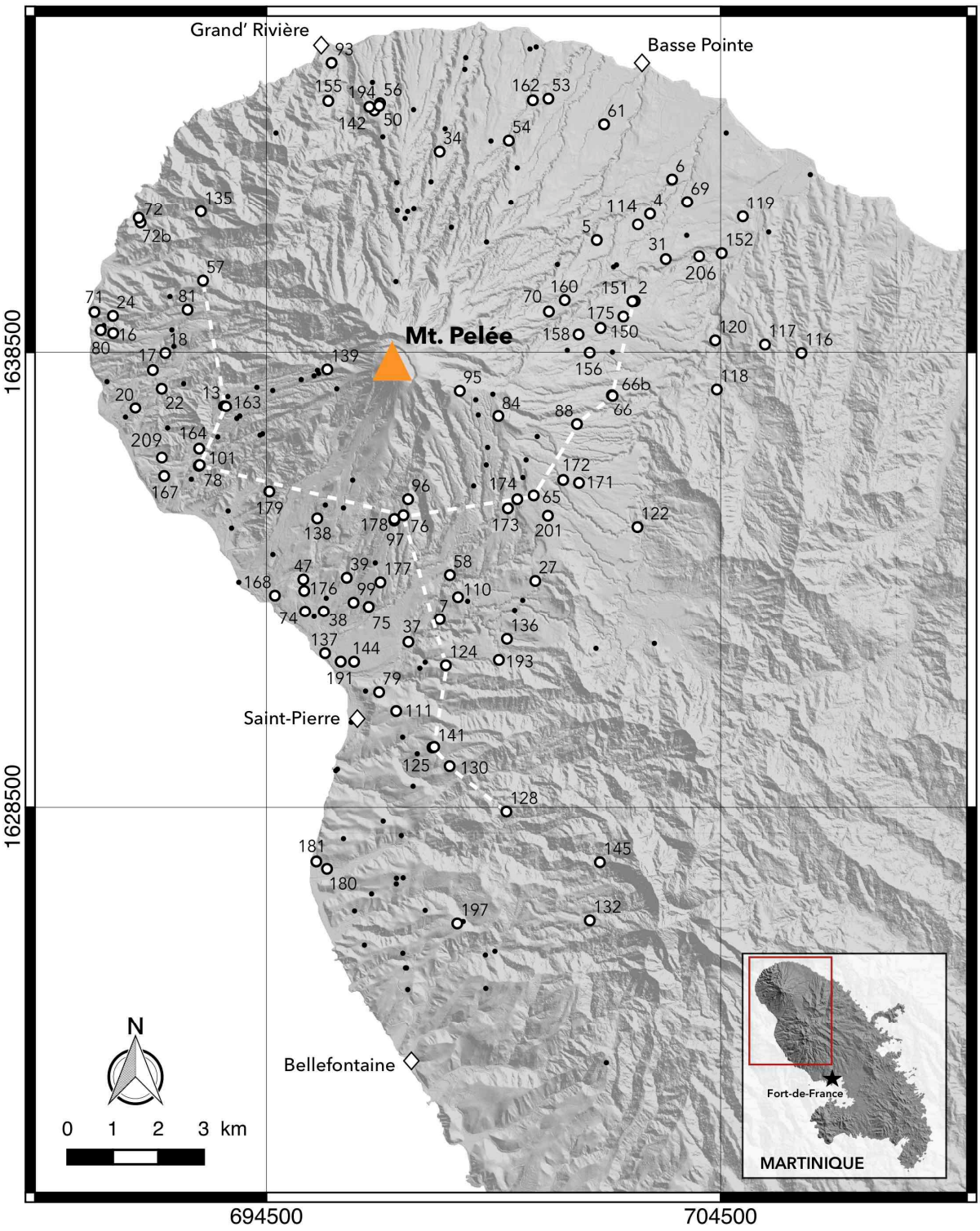
Grand' Rivière
Basse Pointe
Mt. Pelée
Saint-Pierre
Bellefontaine
Fort-de-France
MARTINIQUE
N
0 1 2 3 km
1638500
1628500
694500
704500

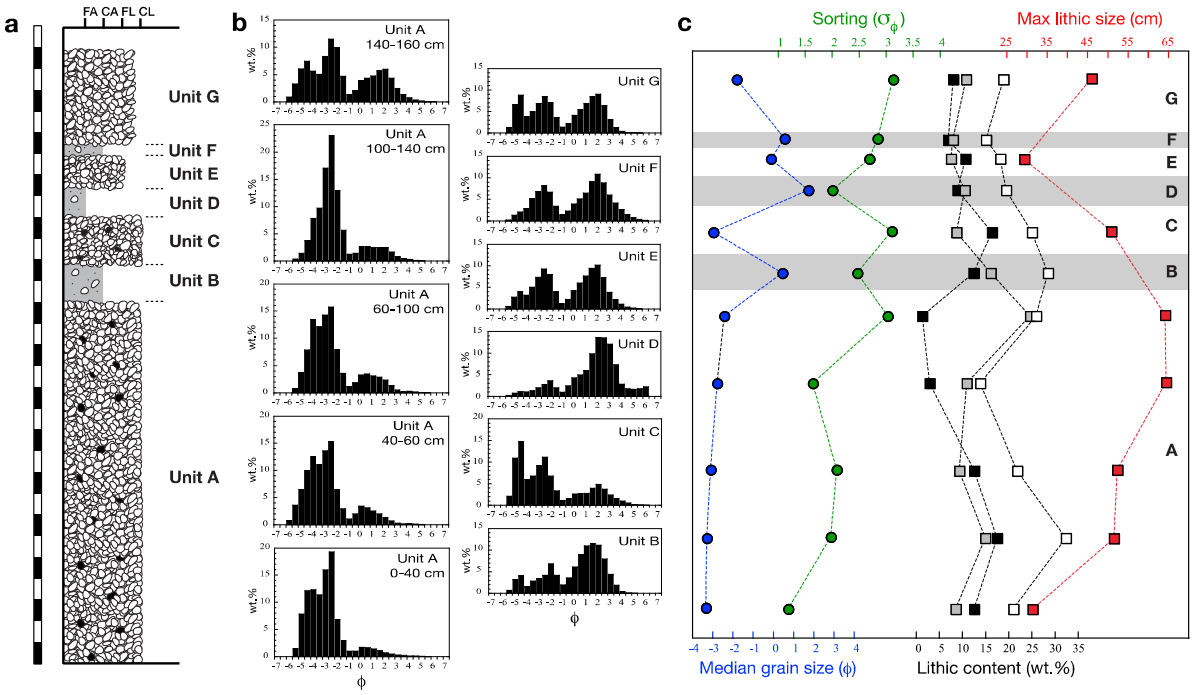
a
FA CA FL CL
Unit G
Unit F
Unit E
Unit D
Unit C
Unit B
Unit A
b
Unit A 140-160 cm
Unit A 100-140 cm
Unit A 60-100 cm
Unit A 40-60 cm
Unit A 0-40 cm
Unit G
Unit F
Unit E
Unit D
Unit C
Unit B
wt.%
ϕ
c
Sorting (σϕ)
Max lithic size (cm)
Median grain size (ϕ)
Lithic content (wt.%)
G
F
E
D
C
B
A


a
G
F
E
D
C
B
A
b
G
F
E
D
C
B
A
c
G
F
E
D
C
B
A
d
P1
650 +/- 20 y.B.P.
P2
1670 +/- 40 y.B.P.
C+E+G
A
e
E
D
C
B
A
f
G
F
E
D
C

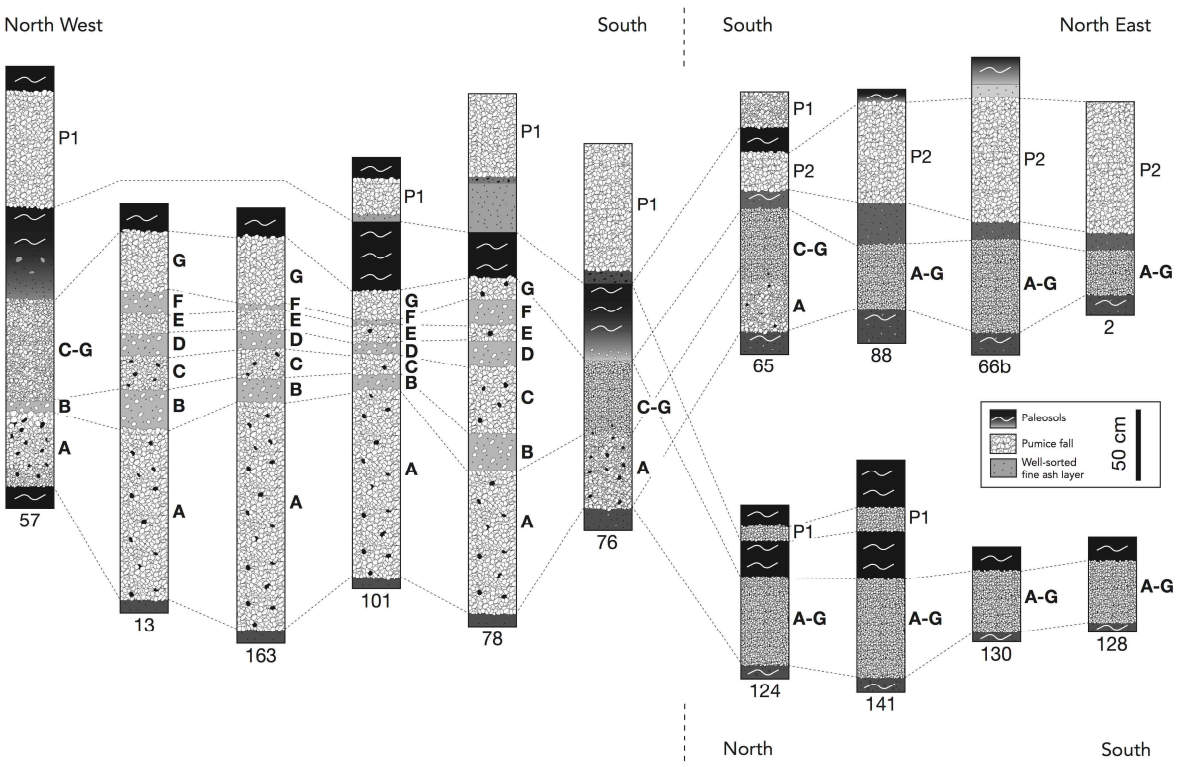
North West
South
South
North East
P1
C-G
B
A
57
G
F
E
D
C
B
A
13
G
F
E
D
C
B
A
163
P1
G
F
E
D
C
B
A
101
P1
G
F
E
D
C
B
A
78
P1
C-G
A
76
P1
P2
C-G
A
65
P2
A-G
88
P2
A-G
66b
P2
A-G
2
P1
A-G
124
P1
A-G
141
A-G
130
A-G
128
Paleosols
Pumice fall
Well-sorted fine ash layer
50 cm
North
South

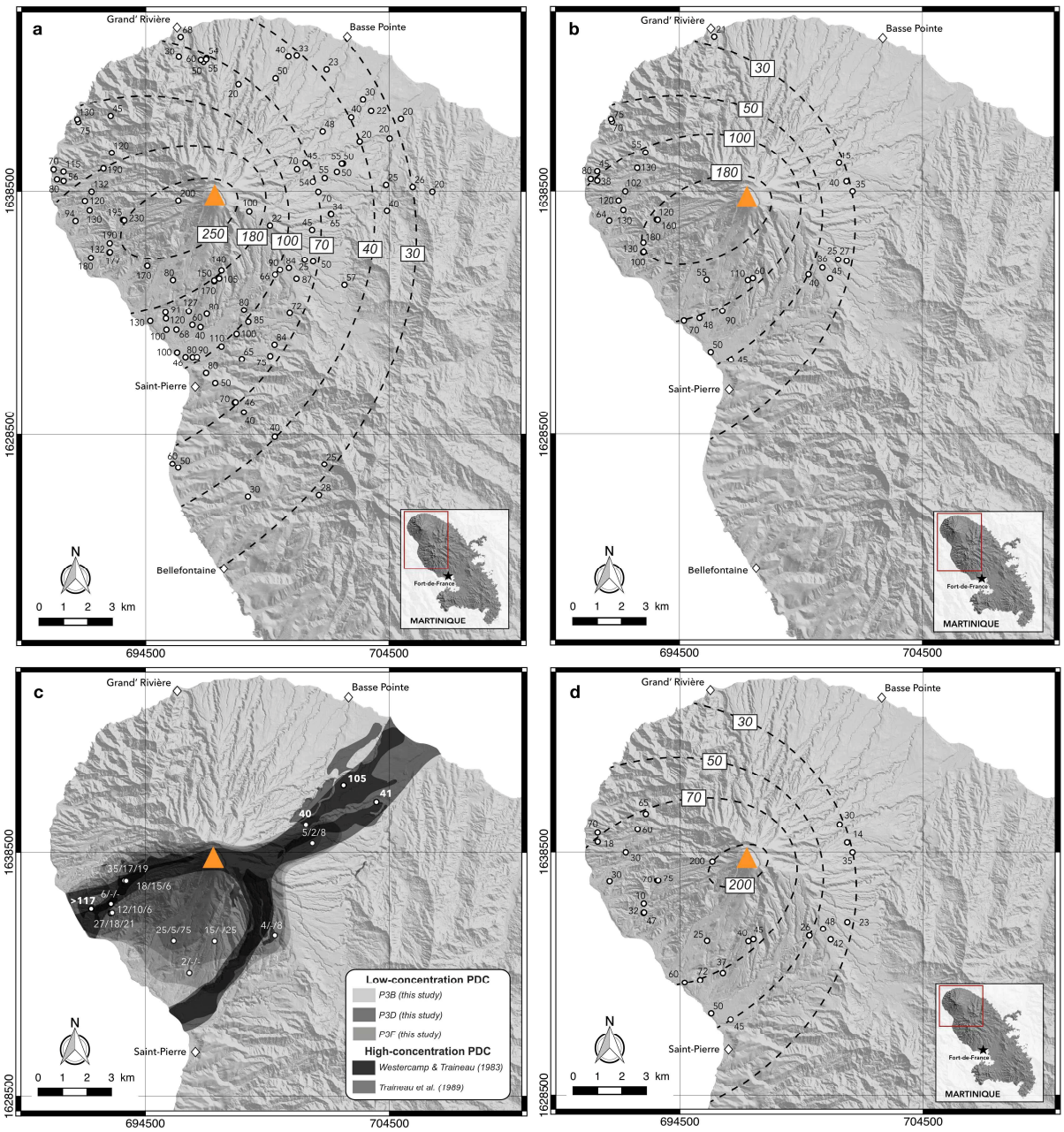
a
Grand' Rivière
Basse Pointe
Saint-Pierre
Bellefontaine
250
180
100
70
40
30
N
0 1 2 3 km
MARTINIQUE
Fort-de-France
1638500
1628500
694500
704500
b
Grand' Rivière
Basse Pointe
30
50
100
180
Saint-Pierre
Bellefontaine
N
0 1 2 3 km
MARTINIQUE
Fort-de-France
1638500
1628500
694500
704500
c
Grand' Rivière
Basse Pointe
105
41
40
5/2/8
35/17/19
18/15/6
>117
12/10/6
27/18/21
25/5/75
15/-/25
4/-/8
2/-/-
Saint-Pierre
N
0 1 2 3 km
Low-concentration PDC
P3B (this study)
P3D (this study)
P3Г (this study)
High-concentration PDC
Westercamp & Traineau (1983)
Traineau et al. (1989)
1638500
1628500
694500
704500
d
Grand' Rivière
Basse Pointe
30
50
70
200
Saint-Pierre
N
0 1 2 3 km
MARTINIQUE
Fort-de-France
1638500
1628500
694500
704500

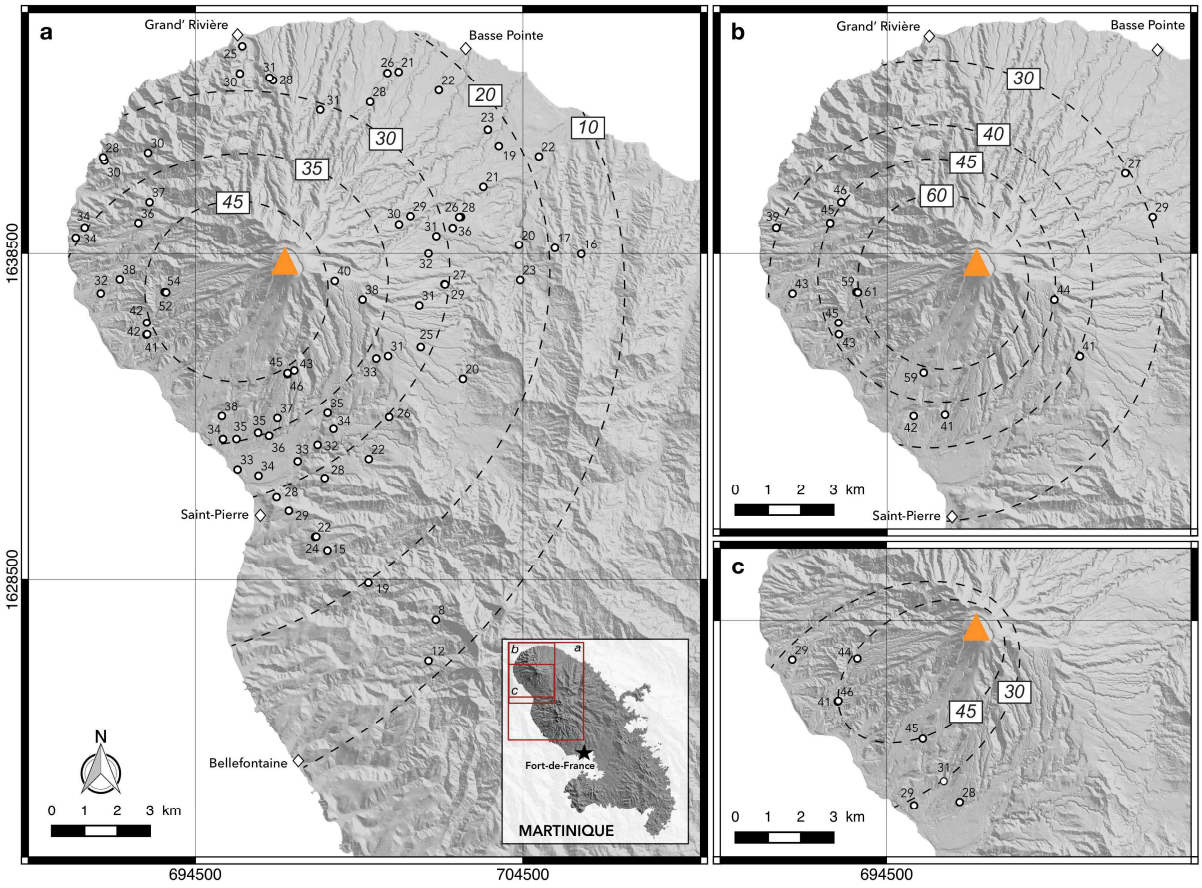
a
Grand' Rivière
Basse Pointe
Saint-Pierre
Bellefontaine
Fort-de-France
MARTINIQUE
N
0 1 2 3 km
1638500
1628500
694500
704500
b
Grand' Rivière
Basse Pointe
Saint-Pierre
0 1 2 3 km
c
0 1 2 3 km
694500

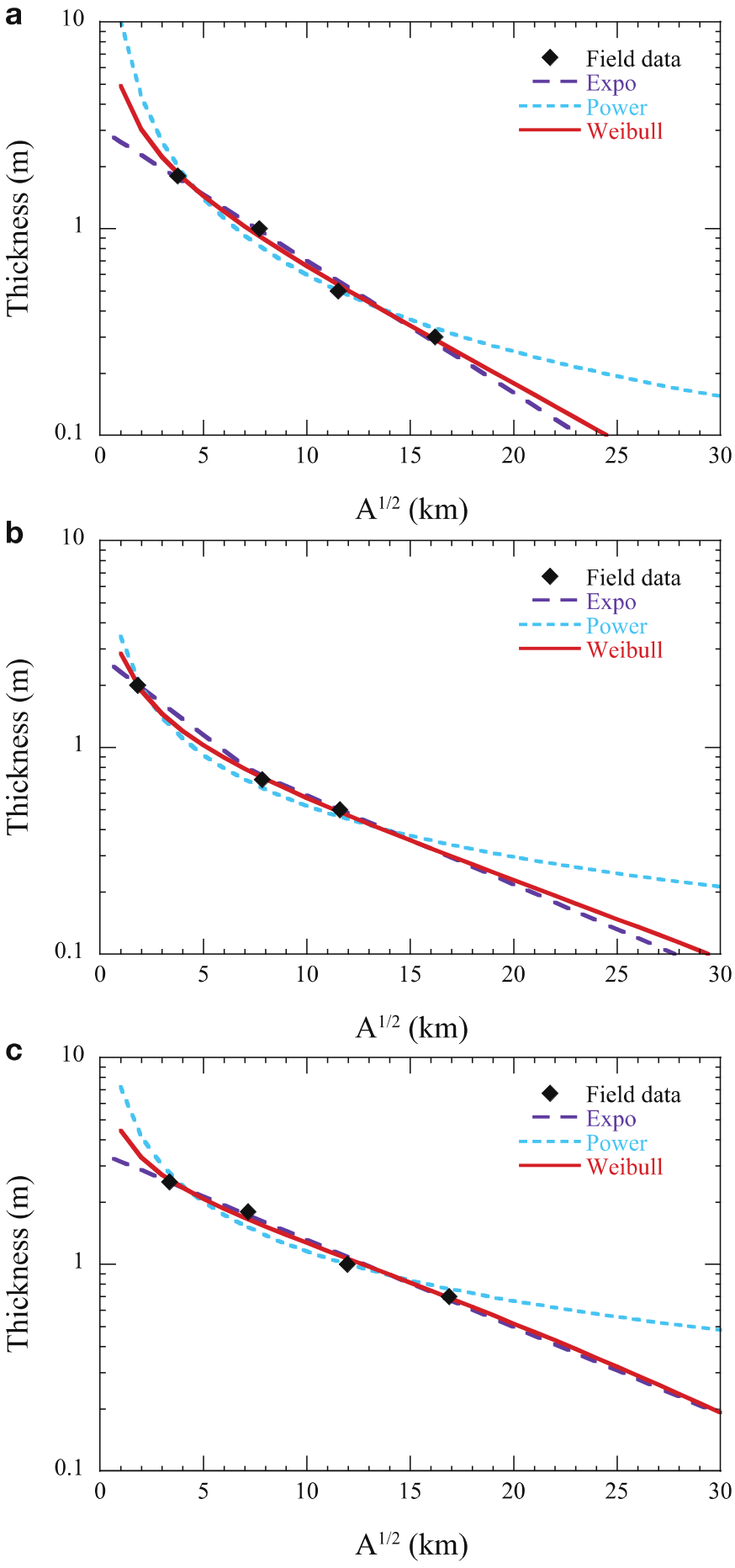
a
b
c
Thickness (m)
A^1/2 (km)
Field data
Expo
Power
Weibull
10
1
0.1
0
5
10
15
20
25
30

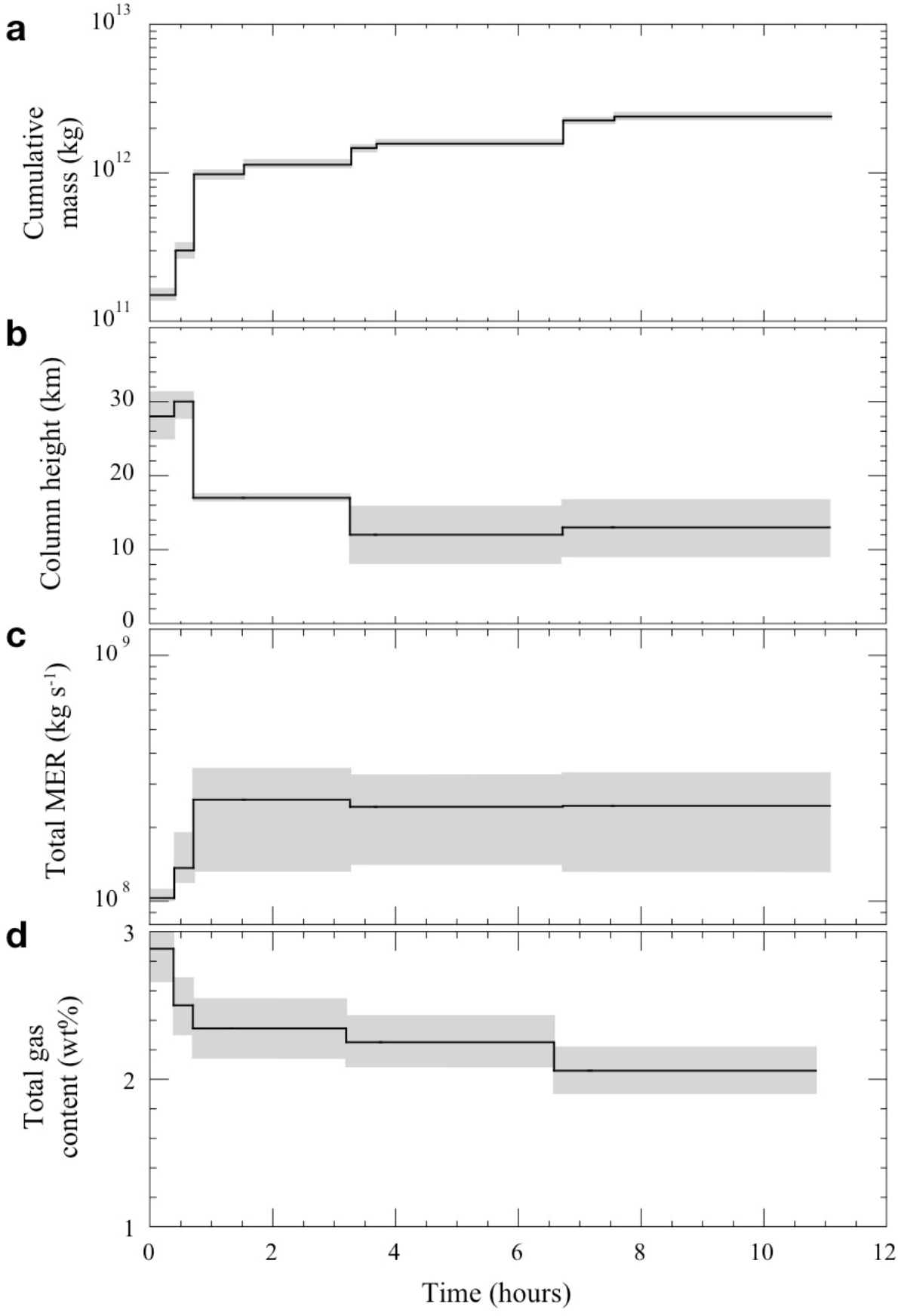
a
b
c
d
Cumulative mass (kg)
Column height (km)
Total MER (kg s-1)
Total gas content (wt%)
Time (hours)
10^13
10^12
10^11
30
20
10
0
10^9
10^8
3
2
1
0
2
4
6
8
10
12

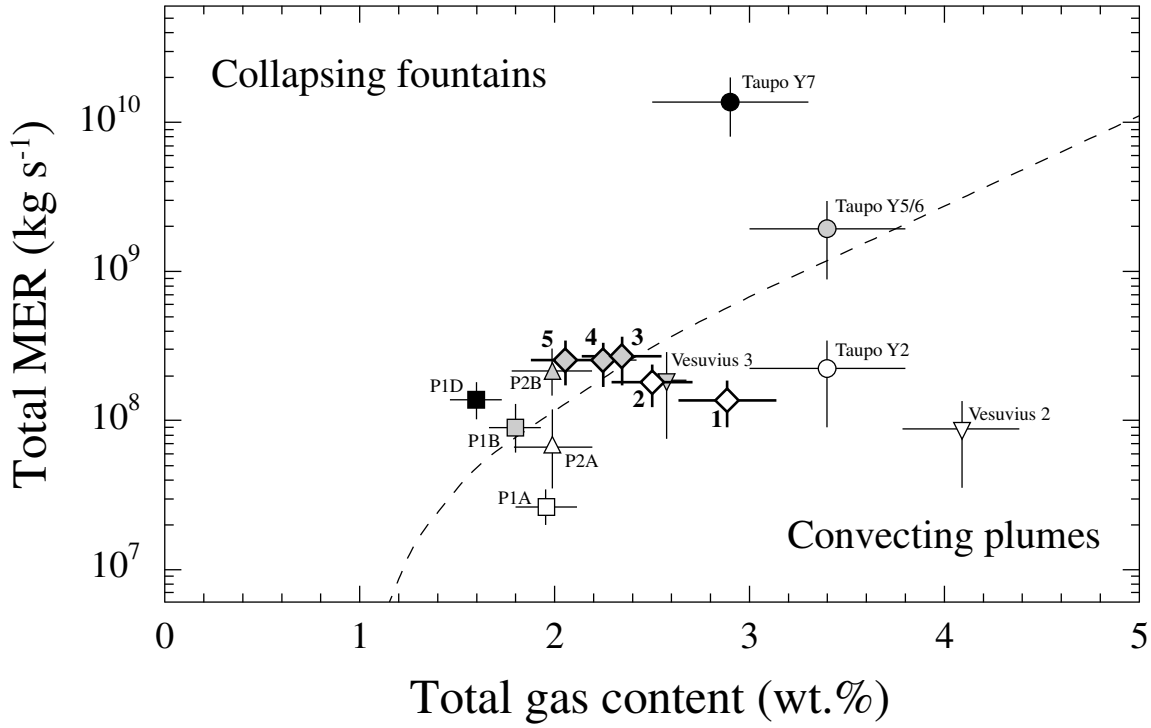
Collapsing fountains
Convecting plumes
Taupo Y7
Taupo Y5/6
Taupo Y2
Vesuvius 3
Vesuvius 2
P1D
P2B
P1B
P2A
P1A
1
2
3
4
5
Total MER (kg s-1)
Total gas content (wt.%)
10^10
10^9
10^8
10^7
0
1
2
3
4
5